Magnetization and transport currents in thin superconducting films

E. Zeldov
Physics Department, The Weizmann Institute of Science, Rehovot 76100, Israel

John R. Clem
Ames Laboratory and Department of Physics and Astronomy, Iowa State University, Ames, Iowa 50011

M. McElfresh and M. Darwin
Physics Department, Purdue University, West Lafayette, Indiana 47907
(Received 27 July 1993)

The critical-state behavior of an infinitely long type-II superconducting thin-film strip is theoretically analyzed for an arbitrary sequence of applied transport currents and perpendicular magnetic fields. Included are solutions for applied field only, transport current only, transport current applied to a sample initially in the remanent critical state, ac applied field, ac transport current, and simultaneously applied field and transport current. The results are compared side by side with corresponding solutions for the more familiar slab geometry; there are striking differences in behavior.

I. INTRODUCTION

New experimental methods recently have been developed to image and measure inhomogeneous magnetic flux distributions and hysteretic flux penetration in type-II superconductors. For example, magneto-optic measurements[1–5] have produced images of the magnetic flux penetration behavior in high-temperature superconductor (HTSC) platelet crystals and thin films. Miniature Hall sensors have been used[6–9] to measure flux penetration behavior in crystals and films including the effect of transport current on the local magnetization. Scanning Hall probes[10,11] were used to obtain the local magnetic-field profiles in HTSC single crystals which even allow for single vortex spatial resolution.[12] In addition, the microscopic Hall-sensor array promises to be a very sensitive tool for investigation of flux penetration and vortex dynamics in films and thin crystals.[13–15] Because of the importance of thin-film applications of the high-temperature superconductors, there currently is considerable interest in the hysteretic magnetic behavior of thin superconducting films. While the hysteretic properties of bulk type-II superconducting samples are reasonably well understood, a good theoretical understanding of the corresponding properties of thin films so far has been lacking. The purpose of this paper is therefore to introduce a theoretical framework for the calculation of hysteretic magnetic fields and electrical current distributions, so that such results can be applied in the analysis of future scanning Hall-probe or magneto-optical experiments with improved field sensitivity and spatial resolution.

The origin of the magnetic hysteresis of type-II superconductors subjected to quasistatic changes of applied magnetic fields and transport currents has long been understood in terms of critical-state theory.[16,17] The basic concepts involved in this theory are as follows. The penetration of magnetic flux into type-II superconductors occurs via quantized vortices (fluxons), which nucleate at the surface when the surface field is high enough. The macroscopic magnetic-field flux density $\mathbf{B}$ in the superconductor ($\mathbf{B}$ is the average of the local magnetic flux density $\mathbf{b}$ over a few intervortex spacings) has magnitude $B = n\phi_0$, where n is the local density of vortices (number per unit area) and $\phi_0 = hc/2e = 2.07 \times 10^{-7}$ G cm^2 is the flux quantum.

The thermodynamic driving force per unit volume on such a vortex array is $\mathbf{F} = \mathbf{J} \times \mathbf{B}/c$, where $\mathbf{J}$ is the coarse-grained current density defined via $\mathbf{J} = (c/4\pi)\nabla \times \mathbf{H}$. Here, the thermodynamic magnetic field $\mathbf{H}$, a function of the flux density $\mathbf{B}$, is defined in terms of the free-energy density $F(B)$ via $\mathbf{H} = 4\pi\partial F/\partial \mathbf{B}$. In isotropic materials, the minimum and maximum values of $H(B)$ in the mixed state are $H(0) = H_{c1}$, the lower critical field, and $H(H_{c2}) = H_{c2}$, the upper critical field. In the absence of surface-barrier or surface-pinning effects,[18] $\mathbf{B}$ and $\mathbf{H}$ satisfy the well known boundary conditions that the normal component of $\mathbf{B}$ and the tangential component of $\mathbf{H}$ are continuous.

When the magnitude of the Lorentz force density $\mathbf{F} = \mathbf{J} \times \mathbf{B}/c$ exceeds the maximum pinning force density $F_p = J_c B/c$, the vortices move in the general direction of $\mathbf{F}$. The resulting vortex motion relaxes the vortex distribution, such that the vortex density $\mathbf{B}$ becomes more uniform and the magnitude of $\mathbf{J}$ decreases. Flux motion generally ceases as J approaches J_c. The critical-current density J_c, a function of B, is an extrinsic property of the superconductor depending upon the distribution of metallurgical defects that locally pin the vortex cores.

To simplify the analysis of flux penetration into a type-II superconductor, various assumptions often are made. One of these, which we use in this paper, is that the current density $\mathbf{J}$ has only one component. As shown in

Fig. 1, when a slab or film (width $2W$) that is infinite in the y direction is considered, and currents and magnetic fields are applied only parallel to the y and z directions, respectively, the current-density vector has only one component,

$$J_y = -\frac{c}{4\pi}\left(\frac{\partial H_z}{\partial x} - \frac{\partial H_x}{\partial z}\right). \quad (1)$$

When the slab is also infinite in the z direction, the situation is further simplified, because H_x is then zero by symmetry, and only the first term on the right-hand side of Eq. (1) contributes to the Lorentz force on the vortices. On the other hand, if the height d of the sample in the z direction becomes very small, as in thin-film geometry ($d \ll W$), the second term on the right-hand side of Eq. (1) becomes increasingly important. One way to think of this term is that it arises from the bending of the vortices that penetrate through the film. However, in the limit of very thin films when the vortices are essentially two dimensional and the current density is nearly uniform across the sample thickness, it is better to think of this term as arising from the fact that the exterior magnetic field wraps around the sample and has tangential components H_x of opposite sign on the top and bottom of the sample $[H_x(x, z = -d/2) = -H_x(x, z = +d/2)]$. Continuity of $H_x(x, z)$ at $z = \pm d/2$ thus requires a large gradient of $\partial H_x/\partial z$ across the sample thickness.

As discussed in Refs. 1, 19–22, it is nearly always the case in thin-film geometry that the first term on the right-hand side of Eq. (1) can be neglected relative to the second term. While space does not permit a detailed discussion of this point, the basic reason for this is the strong demagnetization effects that occur in film geometry. The approximation that $J_y = (c/4\pi)(\partial H_x/\partial z)$ for a thin film then makes it possible to obtain analytic solutions for numerous hysteretic states of thin films.

For simplicity, in this paper we also make two additional assumptions that are commonly made in examining the basic physics of the critical-state model. The first of these is that J_c is a constant, independent of B. The other simplifying assumption is that $\mathbf{H} = \mathbf{B}$. This approximation can be justified in high-κ superconductors, for which $H_{c1} \ll H_{c2}$, in the flux-density range $B > H_{c1}$. Under these conditions the free-energy density in the mixed state is primarily magnetic in origin, such that $F \approx B^2/8\pi$ and $\mathbf{H} = 4\pi\partial F/\partial \mathbf{B} \approx \mathbf{B}$.

The basic equations for the current density used in this paper therefore are

$$J_y(x) = -\frac{c}{4\pi}\frac{\partial B_z(x)}{\partial x} \quad (2)$$

for a slab that is infinite in both the y and z directions (Fig. 1) and

$$J_y(x) = \frac{c}{4\pi d}[B_x(x, z = d/2) - B_x(x, z = -d/2)] \quad (3)$$

for a film that is infinite in the y direction, $J_y(x)$ here representing the current density averaged across the film thickness d.

The use of Eq. (3), which assumes that the first term on the right-hand side of Eq. (1) is negligible, sometimes leads to solutions[9,23–25] for which $\partial B_z/\partial x$ has inverse square-root divergences, a behavior that violates the above assumption. Such vertical slopes in the field profiles therefore are not physically meaningful. Including the first term on the right-hand side of Eq. (1) as a correction term would remove such divergences and change them to profiles with finite slope (as in slab geometry) on a length scale Δx typically of order d, the film thickness ($d \ll W$).

Our goal in this paper is to describe various situations in which it is possible to obtain analytic solutions for the critical states of thin films subjected to applied perpendicular fields and transport currents. To assist the reader in visualizing these cases, we illustrate both the similarities and striking differences in behavior between thin-film and slab geometries. While our results for the thin-film case may appear to be familiar because of their resemblance to those in slab geometry, they are completely new, except that Norris[23] was the first to derive the results for an applied transport current, and Brandt *et al.*[24] and Brandt and Indenbom[25] (whose work we learned of in a report received in the final stages of preparation of this manuscript) recently solved many of the same problems considered here. We first treat, in Secs. II and III, the response to applied magnetic fields and transport currents. This will lay the theoretical groundwork for a general understanding of magnetic hysteresis in thin films. In Sec. IV we consider the more complex case in which a sample, initially in the remanent critical state, is subjected to a transport current, and in Sec. V we treat the response to alternating fields and currents. In Sec. VI we examine the monotonic penetration of flux fronts under increasing applied fields and transport currents. We propose in Sec. VII several approaches to the difficult problem of critical-state current and field with history of applied fields and transport currents. Finally, we summarize our results in Sec. VIII.

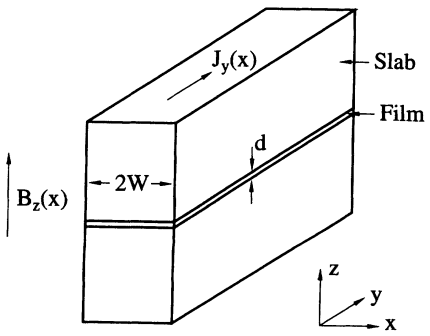

FIG. 1. Schematic diagram of slab and film geometries considered in this paper. The origin of our coordinate system is at the center of the slab or film.

II. RESPONSE TO AN APPLIED MAGNETIC FIELD

We consider here both an infinite type-II superconducting slab and a long superconducting thin-film strip. Both the slab and the film have width $2W$ along the x axis and extend in the y direction, so that the film can be regarded as just a slice of thickness d of the infinite slab shown in Fig. 1. We assume the width of the slab or strip $2W$ to be much larger than the penetration depth λ. We initially consider the response when a magnetic field B_a is gradually applied along the z axis, and later we examine the behavior when a transport current is applied along y. We first analyze the situation where the magnetic field is applied starting from the virgin state in which $B = 0$ everywhere.

In slab geometry, application of the magnetic field B_a induces a diamagnetic current along both surfaces, thereby shielding the interior of the superconductor. When B_a is less than the lower critical field H_{c1}, this screening current flows only within about λ of the surface and decays exponentially beyond this. However, when $B_a \gg H_{c1}$ in a high-κ type-II superconductor (the case considered here), many vortices penetrate into the sample, and ignoring the distinction between $\mathbf{B}$ and $\mathbf{H}$ introduces little error. In this case, the current density can be calculated to good approximation from $\nabla \times \mathbf{B} = 4\pi\mathbf{J}/c$, which in slab geometry reduces to

$$\frac{dB_z(x)}{dx} = -\frac{4\pi}{c} J_y(x). \tag{4}$$

In the critical-state model,[16,17] the current density $\mathbf{J}$ entering the Lorentz force is calculated from $\nabla \times \mathbf{H} = 4\pi\mathbf{J}/c$, where $\mathbf{H}$ is the internal magnetic field in equilibrium with the magnetic flux density $\mathbf{B}$. In the critical state, the magnitude of $\mathbf{J}$ equals the critical-current density J_c. As stated above, however, here we restrict our attention to flux densities sufficiently high that the distinction between $\mathbf{B}$ and $\mathbf{H}$ can be ignored. Assuming for simplicity that J_c is field independent, as in the Bean model,[16,18] one thus obtains from Eq. (4) the following critical-state profiles in slab geometry:

$$J_y(x) = \begin{cases} J_c, & -W < x < -a, \\ 0, & |x| < a, \\ -J_c, & a < x < W, \end{cases} \tag{5}$$

$$B_z(x) = \begin{cases} 0, & 0 \le |x| < a, \\ \frac{4\pi}{c}(|x| - a)J_c, & a \le |x| < W, \\ B_a, & |x| \ge W, \end{cases} \tag{6}$$

where the field-free region of width $2a$ is given by

$$a = W\left(1 - \frac{B_a}{B_s}\right). \tag{7}$$

The vortices penetrate to the center of the slab at a characteristic applied field value B_s given by

$$B_s = \frac{4\pi}{c} W J_c. \tag{8}$$

Figures 2(a) and 2(b) show the corresponding current and field distributions for various B_a values. When $B_a < B_s$, the volume of the slab is divided into regions of two types: a "field-free" region or, more generally, a "field-invariant" region if we start from a nonvirgin state, and "critical" regions. In the field-free region in the center of the slab, $B = 0$ independent of B_a, and the region is characterized by $\mathbf{J} = 0$. The critical regions are characterized by $|\mathbf{J}| = J_c$, and the field here is determined by J_c and B_a. Changes in the applied field displace the boundary between the field-free and critical regions.

We now analyze the film geometry using the same concepts. Application of a weak applied field B_a in the z direction induces Meissner screening currents to flow. Although there is no significant penetration of B_z through the film in this vortex-free state, the net magnetic field wraps around the film such that there is a discontinuity in the component of B_x between the top and bottom surfaces of the film. In turn, because of Ampère's law, currents flow in the film, not just within λ of the edges at $+W$ and $-W$, but all the way to the middle of the film. Conformal mapping methods[26,27] can be used to obtain the following expressions for $J_y(x)$, the current density averaged over the film thickness, and $B_z(x)$, the position-dependent flux density perpendicular to the film:

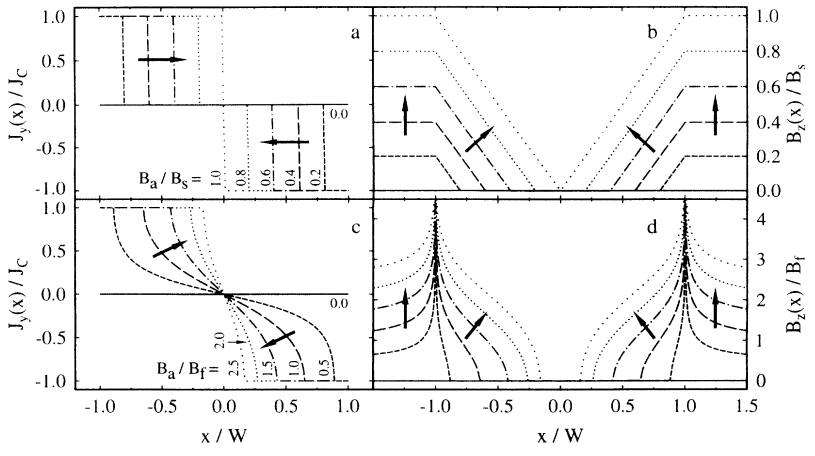

FIG. 2. Calculated critical-state behavior as the applied field B_a is increased for a sample initially in the virgin state. The current-density and magnetic-flux-density profiles for a slab are shown in (a) and (b), and the corresponding profiles for a film are shown in (c) and (d). Arrows indicate the progression of the profiles as B_a increases.

$$J_y(x) = -\frac{cB_a}{2\pi d}\frac{x}{\sqrt{W^2 - x^2}}, \qquad -W < x < W, \tag{9}$$

$$B_z(x) = \frac{B_a|x|}{\sqrt{x^2 - W^2}}, \qquad |x| > W. \tag{10}$$

Equation (9) holds for all $-W < x < W$ except within a narrow region of width λ near the edges if $d > \lambda$. If $d < \lambda$, a modified expression for $J_y(x)$ is needed within a distance Λ of either edge, where $\Lambda = 2\lambda^2/d$ is the two-dimensional screening length.[28–30] We assume in this paper, however, that either $\lambda < d \ll W$ or, if $d < \lambda$, that $d < \lambda < \Lambda \ll W$, such that penetration-depth corrections are needed only in regions of negligible width.

Equation (10) holds for any x outside the film except in a region of width d near the edges if $d > \lambda$ or width Λ if $d < \lambda$. Because of demagnetization effects, the field at the edge of the film is much larger than the applied field. As shown in Ref. 27, if one approximates a film of width $2W$ and thickness d as an ellipse with semimajor axis W and semiminor axis $d/2$, the field at the edge is estimated to be $B_{\rm edge} \simeq (2W/d)B_a$. However, this expression overestimates the field enhancement found experimentally.[15] A more accurate expression is found to be $B_{\rm edge} \simeq \sqrt{W/d}B_a$, which is obtained from Eq. (10) by replacing x by $W + d/2$ and noting that $d \ll W$. A similar expression can be obtained using the approach of Ref. 27 but by choosing the semiminor axis of the ellipse so that the local radius of curvature is $d/2$ at the edge.[31] When $B_{\rm edge}$ exceeds H_{c1}, vortices nucleate at the film's edge and penetrate into the film. The depth to which these vortices penetrate depends upon the strength of pinning; the weaker the pinning, the farther the vortices penetrate. According to the critical-state model,[17] the distribution of vortices in metastable states can be obtained by setting the magnitude of the current density equal to the critical value J_c. Whereas in the case of slab geometry the current density depends almost entirely upon the gradient of $\mathbf{H}$, in film geometry $\mathbf{J}$ depends primarily upon the curvature of $\mathbf{H}$. As discussed in detail in Refs. 1, 19–22, this occurs because of the strong demagnetizing effects that are present in film geometry.

After the vortices penetrate into the film, the condition found in the slab, that $|\mathbf{J}| = J_c$ in the outer region and $\mathbf{J} = 0$ in the central region, does not apply. What is required is a solution for $\mathbf{J}$ and $\mathbf{B}$ for which $B_z = 0$ in a region of width $2a$ in the film's center. The reason for this is that, when either $\lambda < d \ll W$ or, if $d < \lambda$, $d < \lambda < \Lambda \ll W$, the z component of the magnetic flux density is exponentially small except within the appropriate penetration depth of the penetrating vortices. Along the sample edges, $|\mathbf{J}| = J_c$, and the local vortex density $n(x)$ is related to the transverse component of the magnetic field $B_z(x)$ via

$$n(x) = B_z(x)/\phi_0, \tag{11}$$

where $\phi_0 = hc/2e$. By analogy with the three-dimensional (3D) case (slab geometry), the current density J_y must be J_c for $-W < x < -a$ and $-J_c$ for $a < x < W$. As shown by Norris,[23] it is possible to use conformal mapping and the method of images to obtain the current density in the central region $-a < x < a$ arising in response to currents in the flux-penetrated outer region. The image current per unit width that arises in response to a current filament $I = J_c d\Delta x$ at $x = -t$ is

$$-\frac{I}{\pi(t+x)}\sqrt{\frac{t^2 - a^2}{a^2 - x^2}}. \tag{12}$$

Adding to this the image current per unit width that arises in response to a current filament $-I$ at $x = t$, we obtain

$$\frac{2Ix}{\pi(t^2 - x^2)}\sqrt{\frac{t^2 - a^2}{a^2 - x^2}}. \tag{13}$$

Integrating over all the filaments in the constant-J_c region yields the following image-current-density distribution in the region $-a < x < a$:

$$J_{iy}(x) = \frac{2J_c x}{\pi\sqrt{a^2 - x^2}}\ln\frac{\sqrt{W^2 - a^2} + W}{a} - \frac{2J_c}{\pi}\arctan\left(\frac{x}{W}\sqrt{\frac{W^2 - a^2}{a^2 - x^2}}\right). \tag{14}$$

The net current density J_y in the region $-a < x < a$, however, is the sum of J_{iy} and J_{ay}, the current density induced in response to the applied field. J_{ay} is evaluated from Eq. (9) by replacing W by a. As stressed by Norris,[23] J_y must be continuous. Thus we must choose a such that J_{ay} cancels the first term on the right-hand side of Eq. (14). The resulting width $2a$ of the field-free region is given by

$$a = \frac{W}{\cosh(B_a/B_f)}, \tag{15}$$

where

$$B_f = \frac{4}{c}dJ_c \tag{16}$$

is the characteristic field for film geometry. The net current density J_y in the film[24] is therefore

$$J_y(x) = \begin{cases} J_c, & -W < x \le -a, \\ -\frac{2J_c}{\pi}\arctan\left(\frac{x}{W}\sqrt{\frac{W^2-a^2}{a^2-x^2}}\right), & -a < x < a, \\ -J_c, & a \le x < W. \end{cases} \tag{17}$$

This result is analogous to the current distribution obtained by Mikheenko and Kuzovlev[32] for the "thin disk" geometry and consistent with the result obtained by Larkin and Ovchinnikov[30] for a semi-infinitely wide thin film.

The transverse component of the magnetic field is given by

$$B_z(x) = B_a + \frac{2d}{c}\int_{-W}^{W}\frac{J_y(t)}{t - x}dt, \tag{18}$$

which, upon carrying out the required integration, results in

$$B_z(x) = \begin{cases} 0, & -a \le x \le a, \\ B_f \ln \frac{|x|\sqrt{W^2-a^2}+W\sqrt{x^2-a^2}}{a\sqrt{|x^2-W^2|}}, & |x| > a. \end{cases} \tag{19}$$

The apparently infinite slope of $B_z(x)$ as $x \to \pm a$ is an artifact resulting from the use of Eq. (3). Inclusion of the first term on the right-hand side of Eq. (1) would change this behavior to one of linear slope (as in slab geometry) within a distance d of the flux fronts at $x = |a|$. It should be noted that in the limit of small B_a/B_f the width $2a$ of the field-free region becomes nearly equal to the width $2W$ of the strip, and Eq. (17) reduces to Eq. (9) and Eq. (19) reduces to Eq. (10).

Figures 2(c) and 2(d) show the current-density and magnetic-field distributions for various values of the applied field. Note that there are substantial differences in the way a slab and a film respond to an external field. In the critical region, $|x| > a$, the current density obeys $|\mathbf{J}| = J_c$ in both geometries. In the vortex-free region, however, there is a continuous nonzero current density in the film, while $\mathbf{J} = 0$ in a slab. The flux penetration depth increases linearly with B_a in slab geometry, whereas in the film the penetration is strongly nonlinear as given by Eq. (15). Related profiles of the flux penetration into thin films and thin crystals of HTSC's have been recently observed by use of magneto-optic techniques[1–3] and scanning Hall-probe measurements.[10,11]

The magnetization per unit volume in the general case is given by

$$M_z = \frac{1}{2cW}\int_{-W}^{W} x J_y(x)\,dx. \tag{20}$$

It is interesting to note that when $|\mathbf{J}| = J_c$ throughout the sample, the maximum magnitude of the magnetization is the same for both slab and film geometries: $M_{\max} = J_c W/2c$. However, the approach to this value as a function of the applied field is very different in the two geometries. In a slab we obtain

$$\frac{M_z}{M_{\max}} = -\left(1 - \frac{a^2}{W^2}\right) = -\frac{B_a}{B_s}\left(2 - \frac{B_a}{B_s}\right) \tag{21}$$

for $B_a \le B_s$, whereas in a film

$$\frac{M_z}{M_{\max}} = -\sqrt{1-(a/W)^2} = -\tanh(B_a/B_f). \tag{22}$$

III. RESPONSE TO A TRANSPORT CURRENT

We now analyze the distribution of transport current in slab and film geometries in the absence of an applied field. For a slab, a small applied current flows within about λ of each surface ($\lambda \ll W$) and decays exponentially beyond this. When the self-field at the surface exceeds H_{c1}, however, vortices penetrate into the sample to a depth that is determined by the strength of pinning, which in turn is characterized by the critical-current density J_c. As above, we consider only the case of high-κ superconductors and large fields, such that we can ignore the distinction between $\mathbf{B}$ and $\mathbf{H}$. According to the critical-state model, the current density is then

$$J_y(x) = \begin{cases} 0, & -a < x < a, \\ J_c, & a < |x| < W, \end{cases} \tag{23}$$

where $2a$, the width of the central field-free region, is determined by

$$a = W(1 - I_T/I_c). \tag{24}$$

Here I_T is the applied transport current in the y direction per unit height of the slab and $I_c = 2WJ_c$ is the critical current per unit height. Figures 3(a) and 3(b) show current-density and flux-density distributions for various values of I_T. Note that an infinite slab produces a constant magnetic field of $2\pi I_T/c$ on the left of the slab and a negative field of the same intensity on the right.

In film geometry, a weak applied transport current I_T in the y direction generates a self-field that wraps around the sample and produces a discontinuity in the component of B_x between the top and bottom surfaces of the film. Currents therefore flow near the film surface and not just within λ of the edges, but across the entire width of the film. Conformal mapping methods[26,27] can be used to obtain the following expressions for $J_y(x)$, the current density averaged over the film thickness, and $B_z(x)$, the flux density in the plane of the film:

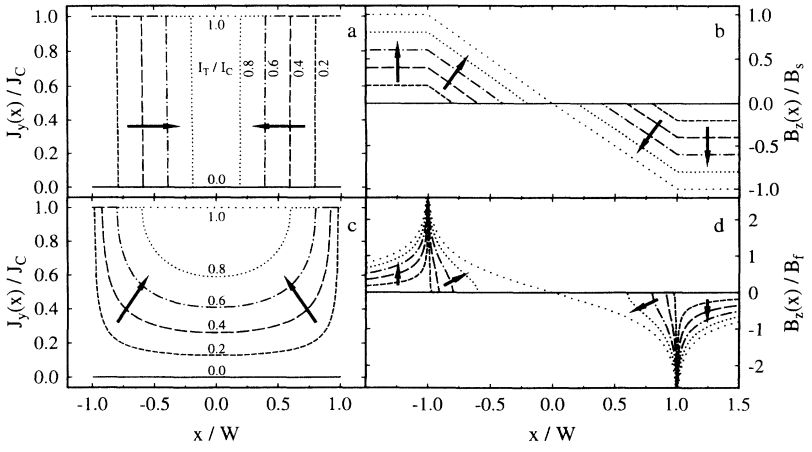

FIG. 3. Calculated critical-state behavior as the transport current I_T is increased for a sample initially in the virgin state. The current-density and magnetic-flux-density profiles for a slab are shown in (a) and (b), and the corresponding profiles for a film are shown in (c) and (d). Arrows indicate the progression of the profiles as I_T increases. The entire cross section finally attains the critical state when $I_T = I_c$.

$$J_y(x) = \frac{I_T}{\pi d\sqrt{W^2 - x^2}}, \qquad -W < x < W, \tag{25}$$

$$B_z(x) = -\frac{2xI_T}{c|x|\sqrt{x^2 - W^2}}, \qquad |x| > W. \tag{26}$$

The field at the edge of the film can be estimated as shown in Ref. 27 by approximating a film of width $2W$ and thickness d as an ellipse with semimajor axis W and semiminor axis $d/2$. The resulting estimate is $B_{\text{edge}} \simeq 4I_T/cd$. However, this expression overestimates the edge field. An experimentally more accurate expression for the field enhancement is $B_{\text{edge}} \simeq 2I_T/c\sqrt{dW}$, which is obtained from Eq. (26) by replacing x by $W + d/2$ and noting that $d \ll W$. A similar expression can be obtained using the approach of Ref. 27 but by choosing the semiminor axis of the ellipse so that the local radius of curvature is $d/2$ at the edge.[31] When B_{edge} exceeds H_{c1}, vortices enter the sample and penetrate to a depth determined by the critical-current density J_c. To obtain the resulting current-density and flux-density profiles, we seek a symmetric solution with $J_y = J_c$ on both edges of the strip and a continuous J_y in a central field-free region. The solution can be obtained by following a procedure[23] similar to that which led to Eq. (14) to first obtain an image-current-density distribution J_{iy} in the field-free region of width $2a$. The integral of the resulting J_{iy} over the cross section of the strip in the region $-a < x < a$ is exactly equal to the negative of $2(W - a)dJ_c$, the current carried by the critical region. The total current density in the region $-a < x < a$ therefore must be the sum of J_y and J_{Ty}, the Meissner-response current density generated by a current I_T in a strip of width $2a$. J_{Ty} is evaluated from Eq. (25) by replacing W by a. Choosing a so that a continuous, nondivergent $J_y(x)$ is obtained, we obtain

$$J_y(x) = \begin{cases} \frac{2J_c}{\pi} \arctan\left(\sqrt{\frac{W^2-a^2}{a^2-x^2}}\right), & -a < x < a, \\ J_c, & a \le |x| < W, \end{cases} \tag{27}$$

where the width of the field-free region $2a$ is determined from

$$a = W\sqrt{1 - (I_T/I_c)^2}, \tag{28}$$

and $I_c = 2dWJ_c$ is the critical current of the strip. Note that, in contrast to the slab case, there is a nonlinear dependence of a upon the transport current I_T.

The transverse component of the magnetic field, obtained by integration using Eqs. (18) (with $B_a = 0$) and (27), is

$$B_z(x) = \begin{cases} 0, & -a \le x \le a, \\ \pm B_f \ln \frac{\sqrt{W^2-x^2}}{\sqrt{W^2-a^2}-\sqrt{x^2-a^2}}, & a < |x| < W, \\ \pm B_f \ln \frac{\sqrt{x^2-W^2}}{\sqrt{x^2-a^2}-\sqrt{W^2-a^2}}, & |x| > W, \end{cases} \tag{29}$$

where B_z is positive (negative) and the upper (lower) sign applies when $x < 0$ ($x > 0$). As discussed in the paragraph following Eq. (19), the diverging slope of $B_z(x)$ as $x \to \pm a$ (as well as in several other similar cases in the following sections) is an artifact that would be removed within a distance d of $x = |a|$ in a more exact analysis. For very small currents it can be shown that Eq. (27) reduces to Eq. (25) and Eq. (29) reduces to Eq. (26).

Figures 3(c) and 3(d) show $J_y(x)$ and $B_z(x)$ for several values of the transport current I_T. The slab and film solutions have some significant differences. The field-free region in the slab is always current free, whereas in the film one may have any value of $|J_y| < J_c$ in the central region where $B_z = 0$. In fact, the field-free region of the film may even carry the majority of the transport current. At $I_T = 0.6I_c$, for example, 60% of the volume of the slab carries transport current with density J_c, and the remaining 40% carries no current at all. On the other hand, in the film at $0.6I_c$ only 20% of the volume carries J_c, whereas the remaining vortex-free region carries 2/3 of the total current with an average density of $0.5J_c$. The width of the field-free region drops linearly with I_T in the slab but has a strongly nonlinear behavior in the film. Comparing the profiles of the magnetic field, we see a linear penetration of the field into the slab, whereas in the strip the field peaks sharply at the edges and drops rapidly toward the center. The magnetic-field profiles due to transport currents in thin HTSC films have recently been measured by use of the magneto-optic technique.[4,5]

IV. SAMPLE IN THE REMANENT STATE: RESPONSE TO A TRANSPORT CURRENT

We now combine our previous results in order to analyze the current and field distributions produced when a transport current is applied to a sample in the remanent state. Here we define the remanent state as the critical state that is produced by first exposing the sample to a very high magnetic field and then reducing the applied field to zero. In this state $J_y(x) = -J_c$ for $-W < x < 0$ and $J_y(x) = J_c$ for $0 < x < W$, as shown by the solid lines in Figs. 4(a) and 4(c). The transport current is now gradually applied in the y direction. The added current cannot flow in the region $x > 0$ because $|J_y|$ cannot exceed J_c in the critical state. All the transport current therefore flows in the region $x < 0$. This additional current changes the profile of the magnetic field and hence the distribution of vortices. However, the vortices move only if $|\mathbf{J}|$ exceeds J_c. Where $|J_y(x)| < J_c$, the driving force is smaller than the maximum pinning force, and the vortices remain immobile. As a result, the volume of the sample is again divided into critical regions where $|J_y(x)| = J_c$ and the field is modified by the transport current, and field-invariant regions where $|J_y(x)| \le J_c$ and the field B_z is equal to its value in the remanent state. In slab geometry, this condition is fulfilled when the added transport current flows symmetrically about the $x = -W/2$ plane with critical density J_c next to $x = -W$ and $x = 0$ as shown in Fig. 4(a). The net current distribution is given by

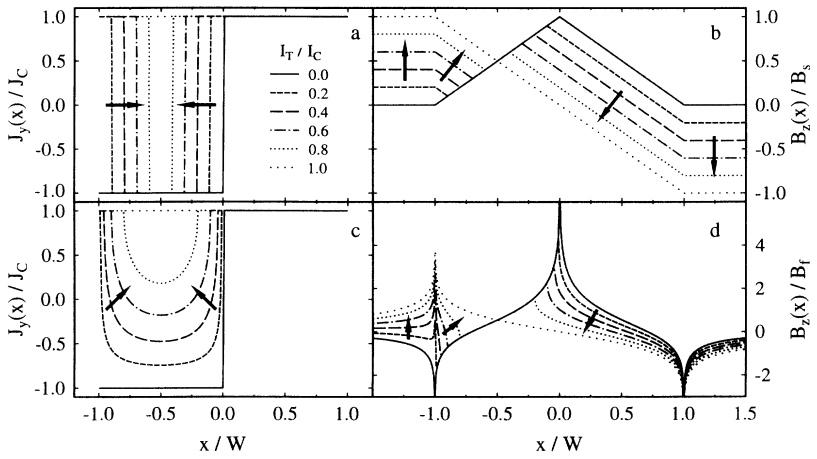

FIG. 4. Calculated critical-state behavior as the transport current I_T is increased for a sample initially in the fully penetrated remanent state. The current-density and magnetic-flux-density profiles for a slab are shown in (a) and (b), and the corresponding profiles for a film are shown in (c) and (d). The solid curves show the initial $I_T = 0$ profiles, and arrows indicate the progression of the subsequent profiles as I_T increases. The entire cross section attains the critical state when $I_T = I_c$.

$$J_y(x) = \begin{cases} J_c, & -W < x < -W/2 - a \quad \text{or} \quad -W/2 + a < x < W, \\ -J_c, & -W/2 - a < x < -W/2 + a. \end{cases} \tag{30}$$

The width $2a$ of the field-invariant region is now given by

$$a = \frac{W}{2}(1 - I_T/I_c), \tag{31}$$

which is half of the value obtained in Eq. (24). Figures 4(a) and 4(b) show the current and field distributions for various values of the transport current in the slab geometry.

In film geometry, application of a transport current results in a net current-density distribution that is the sum of a remanent-flux contribution, $J_{ry}(x) = -J_c$ for $-W < x < 0$ and $J_{ry}(x) = J_c$ for $0 < x < W$, and a transport-current distribution,

$$J_{ty}(x) = \begin{cases} 2J_c, & -W < x \le -W/2 - a \quad \text{or} \quad -W/2 + a \le x \le 0, \\ \frac{4J_c}{\pi} \arctan \sqrt{\frac{(W/2)^2 - a^2}{a^2 - (x + W/2)^2}}, & -W/2 - a < x < -W/2 + a, \\ 0, & 0 \le x < W. \end{cases} \tag{32}$$

Note that the added transport current flows symmetrically about $x = -W/2$, but only in the region $x < 0$. The maximum magnitude of $J_{ty}(x)$ is double that given in Eq. (27), and hence the width $2a$ of the flux-frozen region, given by

$$a = \frac{W}{2}\sqrt{1 - (I_T/I_c)^2}, \tag{33}$$

is half that given by Eq. (28). The net current density is

$$J_y(x) = \begin{cases} J_c, & -W < x \le -W/2 - a \quad \text{or} \quad -W/2 + a \le x < W, \\ \frac{4J_c}{\pi} \arctan\left(\sqrt{\frac{(W/2)^2 - a^2}{a^2 - (x + W/2)^2}}\right) - J_c, & -W/2 - a < x < -W/2 + a. \end{cases} \tag{34}$$

The resulting net current and field distributions are shown in Figs. 4(c) and 4(d). It is striking that in film geometry the current density may change in both magnitude and direction (from nearly $-J_c$ to J_c) while maintaining the same $B_z(x)$ in the flux-frozen region. In slab geometry, on the other hand [Fig. 4(a)], $J_y(x) = -J_c$ in the field-invariant region. This results from Eq. (4), which dictates that field invariance requires current-density invariance in slab geometry. The effect of the transport current on a thin HTSC film in a remanent state has been recently measured by Darwin *et al.*[9] using a miniature Hall sensor.

Because the transport-current contribution J_{ty} does not flow symmetrically about $x = 0$, the magnetization of the sample changes from $M_z = M_{\max}$ in the remanent state to $M_z = 0$ at $I_T = I_c$. Noting that the net current density is the sum of the remanent current-density contribution $J_{ry}(x)$ and the transport-current contribution $J_{ty}(x)$, we may rewrite Eq. (20) in the form

$$M_z = \frac{1}{2cW}\left(2\int_0^W xJ_c dx + \int_{-W}^0 (x + W/2)J_{ty}(x)dx - (W/2)\int_{-W}^0 J_{ty}(x)dx\right). \tag{35}$$

The second term vanishes because $J_{ty}(x)$ is symmetric about $x = -W/2$, and the integral in the third term is just the total transport current I_T. Thus

$$M_z = M_{\max}(1 - I_T/I_c), \tag{36}$$

so that the magnetization drops linearly with increasing transport current I_T in both film and slab geometries.

V. RESPONSE TO ALTERNATING FIELDS AND CURRENTS

So far we have analyzed situations in which the transport current or applied field were changed monotonically. We now generalize our results to account for alternating fields and currents. When the direction of the field or current is changed, the response of the system depends on the previously attained maximum values, which we will denote by the subscript 0. This "memory" is preserved as long as the new values do not exceed the previous maximum values. Once the current or the applied field exceeds *in either direction* the previous absolute maximum values, the system "loses its memory" and behaves monotonically as described in the previous sections.

Suppose, for example, that a zero-field-cooled sample is exposed to an increasing applied field up to a maximum value B_{a0} and the field is then dropped to a lower value, $B_a = B_{a0} - \Delta B_a$. At B_{a0} the current and field distributions follow the results of Sec. II and are shown in Fig. 5 by the solid curves. These distributions are the new initial conditions prior to the change ΔB_a. In slab geometry the width $2a$ of the field-invariant region in decreasing field is given by

$$a = W\left(1 - \frac{\Delta B_a/2}{B_s}\right), \tag{37}$$

where the $\Delta B_a/2$ factor arises from the fact that the new shielding current density has an amplitude $2J_c$ relative to that of the B_{a0} initial conditions. The resulting current distribution is described by

$$J_y(x) = \begin{cases} -J_c, & -W < x < -a, \\ J_c, & -a < x < -a_0, \\ 0, & -a_0 < x < a_0, \\ -J_c, & a_0 < x < a, \\ J_c, & a < x < W, \end{cases} \tag{38}$$

where $a_0 = W(1 - B_{a0}/B_s)$. Once B_a drops below $-B_{a0}$ ($\Delta B_a = 2B_{a0}$), the memory of B_{a0} is erased and the distributions follow Eqs. (5)–(7) with negative values of J_c. This process is depicted in Figs. 5(a) and 5(b). Using Eq. (20) we obtain the following magnetization of the slab in an alternating field:

$$\begin{aligned} \frac{M_z}{M_{\max}} &= -\left(1 - \frac{a_0^2}{W^2}\right) + 2\left(1 - \frac{a^2}{W^2}\right) \\ &= -\left(2 - \frac{B_{a0}}{B_s}\right)\frac{B_{a0}}{B_s} + \left(2 - \frac{\Delta B_a}{2B_s}\right)\frac{\Delta B_a}{B_s}. \end{aligned} \tag{39}$$

In film geometry a similar analysis reveals a nonlinear dependence of the width $2a$ of the field-invariant region, now given by

$$a = \frac{W}{\cosh(\Delta B_a/2B_f)}, \tag{40}$$

and the current and field distributions are described by superposition of oppositely circulating shielding currents,

$$J_y(x) = \begin{cases} -J_c, & -W < x \le -a, \\ J_c\left[1 + \frac{4}{\pi}\arctan\left(\frac{x}{W}\sqrt{\frac{W^2-a^2}{a^2-x^2}}\right)\right], & -a < x \le -a_0, \\ \frac{2J_c}{\pi}\left[2\arctan\left(\frac{x}{W}\sqrt{\frac{W^2-a^2}{a^2-x^2}}\right) - \arctan\left(\frac{x}{W}\sqrt{\frac{W^2-a_0^2}{a_0^2-x^2}}\right)\right], & -a_0 < x < a_0, \\ -J_c\left[1 - \frac{4}{\pi}\arctan\left(\frac{x}{W}\sqrt{\frac{W^2-a^2}{a^2-x^2}}\right)\right], & a_0 \le x < a, \\ J_c, & a \le x < W, \end{cases} \tag{41}$$

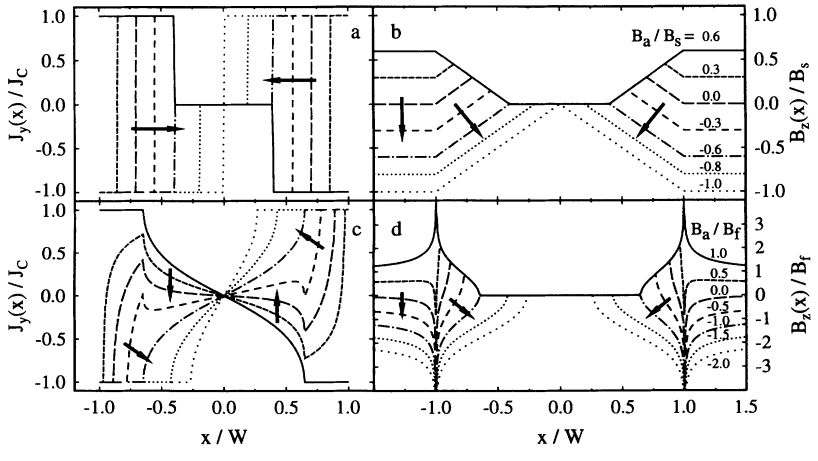

FIG. 5. Calculated critical-state behavior as the applied field B_a is decreased for a sample initially in a partially penetrated state shown in Fig. 2. The current-density and magnetic-flux-density profiles for a slab are shown in (a) and (b), and the corresponding profiles for a film are shown in (c) and (d). The solid curves show the initial $B_a = 0.6B_s$ or $B_a = B_f$ profiles, and arrows indicate the progression of the subsequent profiles as B_a decreases.

$$B_z(x) = \begin{cases} 0, & -a_0 \le x \le a_0, \\ B_f \ln \frac{|x|\sqrt{W^2-a_0^2}+W\sqrt{x^2-a_0^2}}{a_0\sqrt{|x^2-W^2|}}, & a_0 < |x| \le a, \\ B_f \left(\ln \frac{|x|\sqrt{W^2-a_0^2}+W\sqrt{x^2-a_0^2}}{a_0\sqrt{|x^2-W^2|}} - 2\ln \frac{|x|\sqrt{W^2-a^2}+W\sqrt{x^2-a^2}}{a\sqrt{|x^2-W^2|}} \right), & |x| > a, \end{cases} \tag{42}$$

where $a_0 = W/\cosh(B_{a0}/B_f)$. If ΔB_a exceeds $2B_{a0}$, we return again to Eqs. (15), (17), and (19) with the current direction reversed. The magnetization of the strip in decreasing field is given by

$$\frac{M_z}{M_{\max}} = -\sqrt{1-\left(\frac{a_0}{W}\right)^2} + 2\sqrt{1-\left(\frac{a}{W}\right)^2} = -\tanh(B_{a0}/B_f) + 2\tanh(\Delta B_a/2B_f), \tag{43}$$

provided that ΔB_a does not exceed $2B_{a0}$.

The critical-state behavior of a circular thin-film disk in an alternating perpendicular applied magnetic field has been analyzed by Mikheenko and Kuzovlev;[32] an error in Ref. 32 in calculating the superimposed current and field distributions has been corrected by Zhu *et al.*[33] The combined approach of Refs. 32 and 33 has been applied and extended by Clem and Sanchez[34] to calculate the critical-state magnetization M_z of a circular thin-film disk, as well as the corresponding complex ac susceptibility and ac losses.

The critical-state behavior of a thin-film strip has been analyzed recently by Brandt *et al.*[24] and by Brandt and Indenbom,[25] who also have computed the ac losses in an alternating perpendicular applied magnetic field. The results of Eqs. (40)–(43) are in agreement with those of Refs. 24 and 25. Experimentally, the magnetic-field profiles in thin samples exposed to alternating applied fields have been recently measured by use of magneto-optic techniques[2] and scanning Hall sensors.[10]

We now turn to the discussion of alternating transport currents. Similar to the case of alternating fields, the system "remembers" the maximum current as shown in Fig. 6. The current is initially increased to a maximum value I_{T0} and then decreased to $I_T = I_{T0} - \Delta I_T$. In slab geometry we obtain $a_0 = W(1 - I_{T0}/I_c)$ and $a = W(1 - \Delta I_T/2I_c)$ when $\Delta I_T \le 2I_{T0}$. As long as $a > a_0$, the current distribution is similar to the magnetization case of Eq. (38), but with symmetric negative current $J_y = -J_c$ in the outer region $|x| > a$ and positive current $J_y = J_c$ in the region $a_0 < |x| < a$.

In the film the resulting current is a superposition of the distribution given by Eq. (27) arising from I_{T0} and a similar negative term, but with twice the amplitude, arising from ΔI_T:

$$J_y(x) = \begin{cases} \frac{2J_c}{\pi}\left[\arctan\left(\sqrt{\frac{W^2-a_0^2}{a_0^2-x^2}}\right) - 2\arctan\left(\sqrt{\frac{W^2-a^2}{a^2-x^2}}\right)\right], & -a_0 \le x \le a_0, \\ J_c\left[1 - \frac{4}{\pi}\arctan\left(\sqrt{\frac{W^2-a^2}{a^2-x^2}}\right)\right], & a_0 < |x| \le a, \\ -J_c, & a \le |x| < W. \end{cases} \tag{44}$$

The corresponding field is given by

$$B_z(x) = \begin{cases} 0, & -a_0 \le x \le a_0, \\ \pm B_f \ln \frac{\sqrt{W^2-x^2}}{\sqrt{W^2-a_0^2}-\sqrt{x^2-a_0^2}}, & a_0 < |x| \le a, \\ \pm B_f \left[\ln \frac{\sqrt{|x^2-W^2|}}{|\sqrt{x^2-a_0^2}-\sqrt{W^2-a_0^2}|} - 2\ln \frac{\sqrt{|x^2-W^2|}}{|\sqrt{x^2-a^2}-\sqrt{W^2-a^2}|}\right], & |x| > a. \end{cases} \tag{45}$$

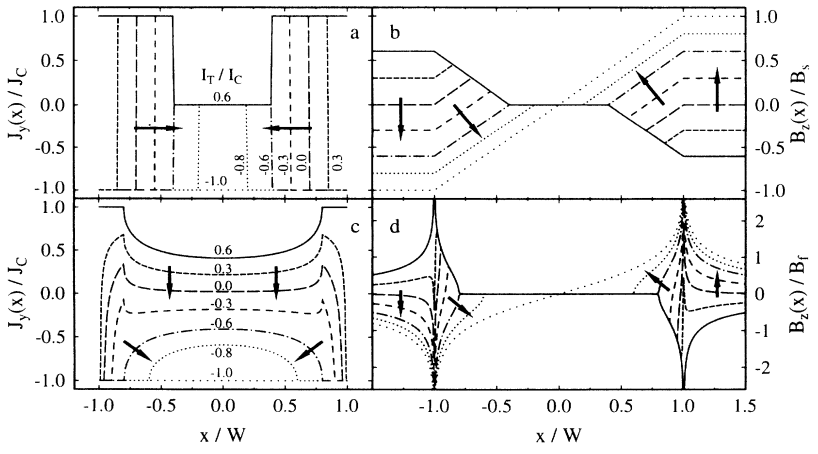

FIG. 6. Calculated critical-state behavior as the transport current I_T is decreased for a sample initially carrying current $I_T = 0.6I_c$ in a partially penetrated state shown in Fig. 3. The current-density and magnetic-flux-density profiles for slabs are shown in (a) and (b), and the corresponding profiles for films are shown in (c) and (d). The solid curves show the initial $I_T = 0.6I_c$ profiles, and arrows indicate the progression of the subsequent profiles as I_T decreases. The entire cross section finally attains the critical state when $I_T = -I_c$.

Here the positive (negative) sign corresponds to $x < 0$ ($x > 0$), $a_0 = W\sqrt{1-(I_{T0}/I_c)^2}$, and $a = W\sqrt{1-(\Delta I_T/2I_c)^2}$. Equations (44) and (45) apply for $\Delta I_T < 2I_{T0}$. If $\Delta I_T > 2I_{T0}$, the memory is erased, and we return to Eqs. (27) – (29) with the direction of the current reversed. Field profiles due to alternating transport currents in films of HTSC's have been observed experimentally by magneto-optic measurements.[5]

An additional case to consider is the application of an alternating transport current to a sample initially in the fully penetrated remanent critical state. In particular, we analyze the situation in which a current is applied to a maximum value I_T and then dropped back to zero. Figure 7 shows the resulting final distributions for various values of the maximum applied current I_T. In slab geometry, as discussed in Sec. IV, the transport current flows in two strips of width $(W/2)(I_T/I_c)$, one adjacent to, but to the right of, $x = -W$ and the other adjacent to, but to the left of, $x = 0$. After the current reaches its maximum value and starts to decrease by ΔI_T, the additional negative current (relative to the peak I_T current) flows in two strips of width $W(\Delta I_T/2I_c)$, one adjacent to, but to the right of, $x = -W$ and the other adjacent to, but to the left of, $x = W$. When the current is reduced back to zero, $I_T = \Delta I_T$, the positive contribution of I_T just to the right of $x = -W$ is canceled because of the linear relation of the current penetration depth. The result is

$$J_y(x) = \begin{cases} -J_c, & -W < x < -W/2 + a \text{ or } W/2 + a < x < W, \\ J_c, & -W/2 + a < x < W/2 + a, \end{cases} \tag{46}$$

where a is given by Eq. (31).

The decreasing transport current flows symmetrically about $x = 0$ and therefore does not reduce the magnetization as long as $\Delta I_T < I_T$. Generally, alternating current will not change the magnetization as long as the current value does not exceed any previous maximum value. The initial magnetization state breaks the symmetry of the transport current flow, and as a result the system remembers the last two extremes of the applied current, the positive and the negative, rather than just the absolute extreme, as in the case of alternating field or current starting from the virgin state. If a positive transport current is raised to I_p, starting from the fully penetrated remanent critical state, and then reduced to zero, the two extremes are I_p and $I_n = 0$. In general, a slab initially in the remanent critical state subjected to a transport current I_T alternating between a positive value I_p and a negative value $-I_n$ has magnetization

$$M_z = M_{\max}\left(1 - \frac{I_n}{I_c}\right)\left(1 - \frac{I_p}{I_c}\right), \tag{47}$$

where $-I_n \le I_T \le I_p$.

In film geometry the situation is different because of the nonlinear penetration depth of the current. For increasing transport current the field-invariant region is given by $a_0 = (W/2)\sqrt{1-(I_T/I_c)^2}$, as in Eq. (33), whereas when the current decreases by ΔI_T, we obtain $a = W\sqrt{1-(\Delta I_T/2I_c)^2}$, as in Eq. (45). The resulting current distribution is

$$J_y(x) = \begin{cases} -J_c\left[1 + \frac{4}{\pi}\arctan\left(\sqrt{\frac{W^2-a^2}{a^2-x^2}}\right) - \frac{4}{\pi}\arctan\left(\sqrt{\frac{(W/2)^2-a_0^2}{a_0^2-(x+W/2)^2}}\right)\right], & -W/2 - a_0 < x < -W/2 + a_0, \\ J_c\left[1 - \frac{4}{\pi}\arctan\left(\sqrt{\frac{W^2-a^2}{a^2-x^2}}\right)\right], & -a < x \le -W/2 - a_0 \text{ or } -W/2 + a_0 \le x < a, \\ -J_c, & a \le |x| < W, \end{cases} \tag{48}$$

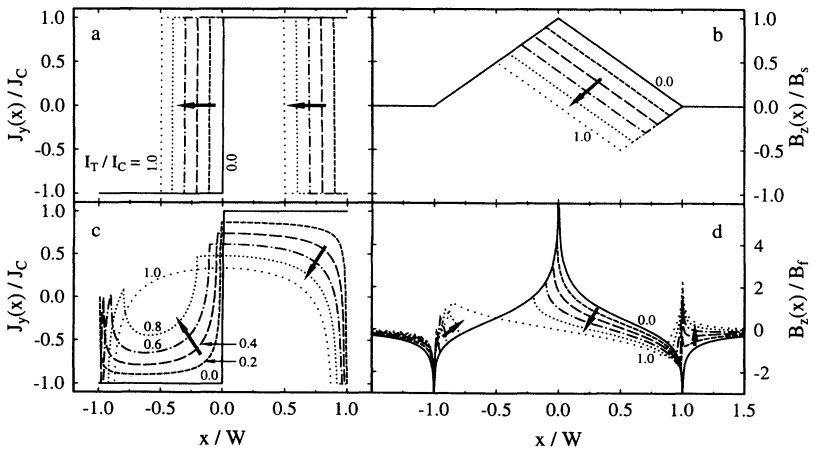

FIG. 7. Calculated critical-state behavior for a sample, initially in a fully penetrated remanent state, to which an applied transport current is raised to an intermediate value I_T and then reduced to zero. The current-density and magnetic-flux-density profiles for slabs are shown in (a) and (b), and the corresponding profiles for films are shown in (c) and (d). The solid curves show the profiles for the remanent state, and arrows indicate the progression of the profiles for increasing intermediate values of I_T. Since the final transport current is zero, the integral of $J_y(x)$ is zero in each case.

which holds for any ΔI_T as long as $a \geq a_0 + W/2$. Figure 7 shows the current and field distributions for various maximum I_T values in the case of zero final transport current, such that $\Delta I_T = I_T$. The fact that the sample is initially in the fully penetrated remanent critical state has a major effect on the final distributions. One can compare the results of Fig. 7 at $I_T = 0.6I_c$, for example, with those of Fig. 6 (curve labeled 0.0), in which the same sequence of transport currents has been applied to a system in the virgin state. The effect of an alternating transport current on the field profile in thin films of HTSC's has been investigated experimentally using miniature Hall sensors.[9]

The effect of an alternating transport current upon the magnetization M_z of the film is similar to that of Eq. (47). However, a much more complicated expression for M_z results because of the nonlinear penetration depth of the current.

VI. ASYMMETRIC CURRENT FLOW: MONOTONIC CASE

In the previous sections we have analyzed the response of the sample to external fields or transport currents applied separately, for the sample initially in the virgin state or in a fully penetrated remanent critical state. All these cases resulted in symmetrical current distributions with the center of symmetry at $x = 0$ or $x = \pm W/2$. In order to determine the response to a general combination of field and current a more detailed analysis must be carried out.

A transport current flowing in the positive y direction results in positive flux penetration on the left side of the sample ($B_z > 0$ for $x < 0$) and a negative flux on the right ($B_z < 0$ for $x > 0$). A magnetic field applied in the positive z direction results in positive flux penetration on both sides of the sample. Clearly, if the current and field are applied simultaneously, the amount of flux penetration on the two sides of the sample will not be equal. In addition, the resulting distributions will depend on the precise sequence of current and field applications. We first analyze the case in which the field and current are increased monotonically starting from a virgin state. For simplicity, we restrict our attention here to $I_T > 0$ and $B_a > 0$, but the results are easily generalized to negative values of I_T and B_a. Assume that the balance between the field and current is such that some positive flux has penetrated from the left ($B_z > 0$) and some negative flux has entered from the right ($B_z < 0$). In slab geometry the resulting current and field distributions will be similar to those shown in Figs. 3(a) and 3(b). However, on each side of the slab the flux penetration depth will be different. Let $-a_L$ denote the flux-front position on the left and a_R that on the right, so that the vortex-free region has a width of $2a = a_R + a_L$ and is centered at $p = (a_R - a_L)/2$. The current distribution is given, therefore, by

$$J_y(x) = \begin{cases} J_c, & -W < x < -a_L, \\ 0, & -a_L < x < a_R, \\ J_c, & a_R < x < W, \end{cases} \tag{49}$$

and the total transport current per unit height of the slab is $I_T = J_c(2W - a_R - a_L)$. This current induces a magnetic field of $\pm 2\pi I_T/c$ outside the slab in addition to the applied field B_a. Using Eq. (4) and requiring zero field in the vortex-free region, we obtain the field profile

$$B_z(x) = \begin{cases} B_a + \frac{2\pi}{c} I_T, & x \leq -W, \\ -\frac{4\pi}{c} J_c(x + a_L), & -W < x < -a_L, \\ 0, & -a_L \leq x \leq a_R, \\ -\frac{4\pi}{c} J_c(x - a_R), & a_R < x < W, \\ B_a - \frac{2\pi}{c} I_T, & x \geq W. \end{cases} \tag{50}$$

Continuity of $B_z(x)$ results in the following relations:

$$\begin{aligned} a_L &= W\left(1 - \frac{B_a}{B_s} - \frac{I_T}{I_c}\right), \\ a_R &= W\left(1 + \frac{B_a}{B_s} - \frac{I_T}{I_c}\right), \\ a &= (a_R + a_L)/2 = W\left(1 - \frac{I_T}{I_c}\right), \\ p &= (a_R - a_L)/2 = WB_a/B_s. \end{aligned} \tag{51}$$

The width $2a$ of the flux-free region depends only on the transport current, as given in Eq. (24), whereas the position of the vortex-free region inside the slab is controlled by the applied field. The corresponding current and field distributions are shown in Figs. 8(a) and 8(b).

The above results were obtained by assuming that the

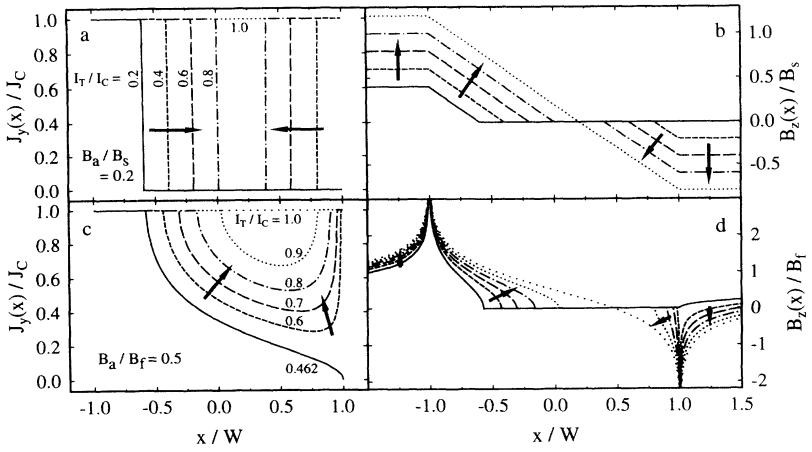

FIG. 8. Calculated critical-state behavior in monotonically increasing field and current in the high-current–low-field regime. The current-density and magnetic-flux-density profiles for slabs are shown in (a) and (b), and the corresponding profiles for films are shown in (c) and (d). The solid curves show the profiles corresponding to the matching conditions of field and current such that no current flows at the right edge of the sample. Arrows indicate the progression of the profiles as I_T is increased which results in generating currents which flow in the same direction on both sides of the sample.

current flows in the same direction on both sides of the sample. This assumption is valid only if $a_R \leq W$ in Eq. (51), i.e.,

$$\frac{I_T}{I_c} \geq \frac{B_a}{B_s}, \tag{52}$$

which means that the magnitude of the self-field induced by the transport current outside the slab must be larger than the magnitude of the applied field. We refer to this as the high-current–low-field regime. The profiles of Figs. 8(a) and 8(b) are applicable to any direction of the field as long as the current is high enough. The condition of high current in Eq. (52) is not sufficient, however, to guarantee these profiles. The final I_T and B_a have to be reached monotonically so that a_R decreases continuously at all times ($da_R/dt \leq 0$). This leads to the limitation

$$\frac{1}{I_c}\frac{dI_T}{dt} \geq \frac{1}{B_s}\frac{dB_a}{dt}. \tag{53}$$

If the field is changed too rapidly, even though Eq. (52) holds, currents in the opposite direction are induced close to the edge of the slab and Eqs. (49) – (51) are invalid.

To find the response of the slab in the low-current–high-field regime, $I_T/I_c \leq B_a/B_s$, we have to start with currents flowing in different directions on opposite sides of the slab. Following the same procedure as above we obtain

$$\begin{aligned} a_L &= W\left(1 - \frac{B_a}{B_s} - \frac{I_T}{I_c}\right), \\ a_R &= W\left(1 - \frac{B_a}{B_s} + \frac{I_T}{I_c}\right), \\ a &= W\left(1 - \frac{B_a}{B_s}\right), \\ p &= WI_T/I_c. \end{aligned} \tag{54}$$

In this regime the roles of the current and the field are interchanged; the width of the flux-free region is now determined by the field, and its position is shifted by the current. The monotonic condition in this regime is exchanged as well and requires $(dB_a/dt)/B_s \geq (dI_T/dt)/I_c$. Some representative current and field distributions for the low-current–high-field regime are shown in Figs. 9(a) and 9(b).

The magnetization of the slab is determined by integrating the current distribution using Eq. (20). In the monotonic high-current–low-field regime the current distribution is given by Eqs. (49) and (51) and the resulting magnetization is

$$\frac{M_z}{M_{\max}} = -2\frac{B_a}{B_s}\left(1 - \frac{I_T}{I_c}\right). \tag{55}$$

Note that this relation holds only for $I_T/I_c \geq B_a/B_s$.

In the low-current–high-field regime the current flows in different directions on opposite sides of the slab, and the current distribution is determined by the parameters given in Eq. (54). The magnetization in this case is

$$\frac{M_z}{M_{\max}} = -\left[2\frac{B_a}{B_s} - \left(\frac{B_a}{B_s}\right)^2 - \left(\frac{I_T}{I_c}\right)^2\right], \tag{56}$$

which holds only for $B_a/B_s \geq I_T/I_c$. In the absence of transport current the magnetization expression reduces to that of Eq. (21) as expected, while Eqs. (55) and (56) become equivalent at $I_T/I_c = B_a/B_s$. In Eq. (56) the magnetization drops quadratically with current, whereas in the previous cases, such as in Eq. (36), we obtained a linear current dependence. This difference arises from the monotonicity requirement. Equation (36) was obtained for a slab in the remanent critical state, which is equivalent to $B_a = B_s$ with the direction of the current reversed. A transport current applied gradually to a slab in the remanent state fulfills $I_T/I_c < B_a/B_s = 1$ but does not satisfy the rate requirement since $d(I_T/I_c)/dt > d(B_a/B_s)/dt = 0$. Therefore, the situation discussed in Sec. IV is fundamentally different from the monotonic case described here and results in different current distributions and magnetizations. For example, one can compare the current profile of $I_T/I_c = 0.2$ curve in the critical state in Fig. 4(a) with that of $I_T/I_c = 0.2$ and $B_a/B_s = 1.0$ in Fig. 9(a). Although the values of I_T and B_a are equivalent, the distributions are very different because of the differing preparation procedures. In Fig. 9 the field and the current are increased simultaneously and monotonically. On the other hand, in Fig. 4 the current is applied after the field has reached its final value, which results in two

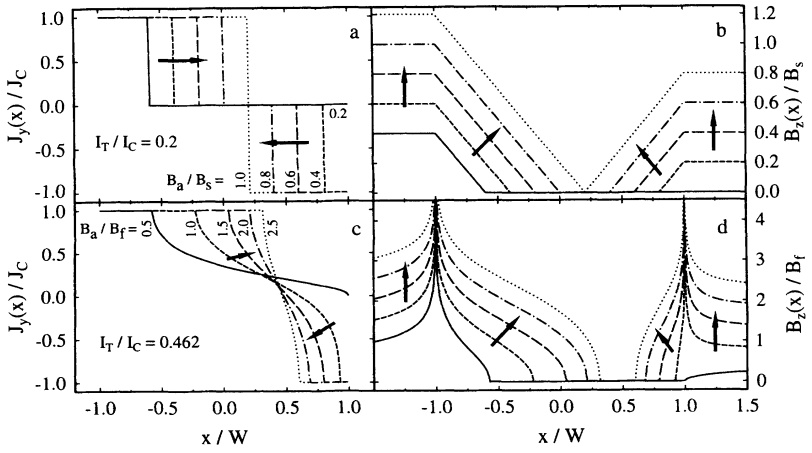

FIG. 9. Calculated critical-state behavior in monotonically increasing field and current in the low-current–high-field regime. The current-density and magnetic-flux-density profiles for slabs are shown in (a) and (b), and the corresponding profiles for films are shown in (c) and (d). The solid curves show the profiles at the same matching conditions as in Fig. 8. Arrows indicate the progression of the profiles as B_a is increased, which results in generating currents that flow in different directions on opposite sides of the sample.

current-direction reversals as compared to one reversal in the monotonic case.

We now derive the response of a thin film under similar external conditions. In the previous sections symmetry was always assumed, and therefore the distribution of current could be obtained by integrating expressions like the one given by Eq. (13). Since this is not the case here, we have to analyze each side of the strip separately. To be more precise in our description, we refer to the critical currents in the flux-penetrated region as the *generating currents* and the associated currents in the vortex-free region as the *image currents*. The distribution of the image currents depends on the distribution of the generating currents and on the width $2a$ of the region that has to be screened. Since the flux-free region is not centered in the middle of the strip, it is convenient to switch to a dimensionless coordinate x' with its origin in the center of the vortex-free region, $x' = (x-p)/a$. The edges of the strip are at $-W_L = -(W+p)/a$ and $W_R = (W-p)/a$, whereas the vortex-free region extends from $x' = -1$ to $x' = 1$. Using Eq. (12) with the new coordinates, the image-current distribution arising from the generating current density J_c between $-W_L$ and -1 is determined by

$$\frac{-J_c}{\pi\sqrt{1-x'^2}}\int_1^{W_L}\frac{\sqrt{t^2-1}}{t+x'}dt = -\frac{J_c\sqrt{W_L^2-1}}{\pi\sqrt{1-x'^2}} + \frac{J_c x'}{\pi\sqrt{1-x'^2}}\ln\left(\sqrt{W_L^2-1}+W_L\right) - \frac{J_c}{\pi}\left(\arcsin\frac{x'W_L+1}{W_L+x'} - \frac{\pi}{2}\right). \quad (57)$$

It is a property of the image currents that their integral across the flux-free region is exactly the negative of the integral of the generating currents across the flux-penetrated region. Thus, at the end of the calculation it will be necessary to add two additional current contributions to the image currents in the flux-free region. The first of these is the Meissner-response current distribution associated with distributing the transport current I_T over the flux-free region, as in Eq. (25), and the second is the Meissner-response current distribution induced by the applied field, as in Eq. (9). The first of these will cancel the first term on the right-hand side of Eq. (57), and the second will cancel the second term on the right-hand side of Eq. (57). We therefore concentrate on the only term remaining at the end of the calculation, the third term on the right-hand side of Eq. (57). This term gives rise to a continuous, nondiverging current-density distribution, which has the value J_c at $x' = -1$ and zero at $x' = 1$.

The above procedure must be repeated for the generating currents on the right side of the strip, assuming first that they flow in the same direction as those on the left side, which corresponds to the high-current–low-field regime,

$$-\frac{J_c}{\pi\sqrt{1-x'^2}}\int_1^{W_R}\frac{\sqrt{t^2-1}}{t-x'}dt = -\frac{J_c\sqrt{W_R^2-1}}{\pi\sqrt{1-x'^2}} - \frac{J_c x'}{\pi\sqrt{1-x'^2}}\ln\left(\sqrt{W_R^2-1}+W_R\right) + \frac{J_c}{\pi}\left(\arcsin\frac{x'W_R-1}{W_R-x'} + \frac{\pi}{2}\right). \quad (58)$$

As discussed above, the net current distribution in the vortex-free region is given by the superposition of the third terms on the right-hand sides of Eqs. (57) and (58). Returning to the original coordinates, we obtain

$$J_y(x) = \begin{cases} \frac{J_c}{\pi}\left(\arcsin\frac{(x-p)(W-p)-a^2}{a(W-x)} - \arcsin\frac{(x-p)(W+p)+a^2}{a(W+x)} + \pi\right), & p-a<x<p+a, \\ J_c, & -W<x\le p-a \text{ or } p+a\le x<W. \end{cases} \quad (59)$$

The corresponding magnetic-field distribution is obtained by use of Eq. (18), which after some manipulations gives

$$B_z(x) = \begin{cases} 0, & p-a\le x\le p+a, \\ \pm\frac{B_f}{2}\ln\left|\frac{(W+x)(\sqrt{[(W-p)^2-a^2][(x-p)^2-a^2]}+(W-p)(x-p)-a^2)}{(W-x)(\sqrt{[(W+p)^2-a^2][(x-p)^2-a^2]}+(W+p)(x-p)+a^2)}\right|, & x>p+a \text{ or } x<p-a, \end{cases} \quad (60)$$

where the upper (lower) sign holds for $x < p-a$ ($x > p+a$). The width of the vortex-free region $2a$ and its position p are determined by the constraints that the total transport current is

$$I_T = d\int_{-W}^{W} J_y(x)dx = dJ_c\left[\sqrt{(W+p)^2-a^2}+\sqrt{(W-p)^2-a^2}\right], \quad (61)$$

and that the currents induced by the applied field cancel the logarithmic terms on the right-hand sides of Eqs. (57) and (58):

$$B_a = \frac{2dJ_c}{c}\ln\frac{\sqrt{(W+p)^2-a^2}+W+p}{\sqrt{(W-p)^2-a^2}+W-p}. \quad (62)$$

The solution is facilitated by introducing the parameters $\beta = \exp(2B_a/B_f), i = I_T/I_c$, and $\omega = \sqrt{(W_L^2-1)}+W_L$. After some algebraic manipulations we obtain $W_L = (1+\omega^2)/(2\omega)$, $W_R = (\beta^2+\omega^2)/(2\beta\omega)$, and $\omega = \sqrt{\beta(1+i)/(1-i)}$, which lead to the following relations between the flux-free-region parameters and the

external field and current:

$$a = \frac{2W}{W_L + W_R} = \frac{W}{\cosh(B_a/B_f)}\sqrt{1-(I_T/I_c)^2} \quad (63)$$

and

$$p = W\frac{W_L - W_R}{W_L + W_R} = W\frac{I_T}{I_c}\tanh(B_a/B_f). \quad (64)$$

These results are in striking contrast to those obtained for slab geometry as given in Eq. (51). The width of the vortex-free region in a slab is determined only by the transport current, and its position is governed by the applied field. Here, both the current and the field cause shrinkage of the vortex-free region, as if they act independently [compare with Eqs. (15) and (28)] and both affect its position. The resulting current and field distributions are shown in Figs. 8(c) and 8(d).

The above results were derived under the assumption that the current flow is in the same direction across the strip (the high-current–low-field regime). The boundary of this regime's range of validity is determined using the condition $W_R = 1$ or $\beta = \omega$. As in slab geometry, the transport current must be large enough, and here the current must satisfy the nonlinear condition

$$I_T/I_c \geq \tanh(B_a/B_f). \quad (65)$$

In addition, we require monotonic application of the current and field so that a_R decreases monotonically with time. Thus, the rate of the current increase must satisfy

$$\frac{d(I_T/I_c)}{dt} \geq \frac{d(B_a/B_f)}{dt}\frac{\sqrt{1-(I_T/I_c)^2}}{\cosh(B_a/B_f)}. \quad (66)$$

We now repeat the procedure for the low-current–high-field regime, for which $I_T/I_c \leq \tanh(B_a/B_f)$, so that the generating currents on the two sides of the strip flow in opposite directions. To obtain the net currents in the vortex-free region we must add the third terms on the right-hand sides of Eqs. (57) and (58) with opposite signs to obtain

$$J_y(x) = \begin{cases} J_c, & -W < x \leq p-a, \\ -\frac{J_c}{\pi}\left(\arcsin\frac{(x-p)(W-p)-a^2}{a(W-x)} + \arcsin\frac{(x-p)(W+p)+a^2}{a(W+x)}\right), & p-a < x < p+a, \\ -J_c, & p+a \leq x < W. \end{cases} \quad (67)$$

The resulting field profile is given by

$$B_z(x) = \begin{cases} 0, & p-a \leq x \leq p+a, \\ \pm\frac{B_f}{2}\ln\left|\frac{(W-x)(\sqrt{[(W+p)^2-a^2][(x-p)^2-a^2]}-(W+p)(x-p)-a^2)}{(W+x)(\sqrt{[(W-p)^2-a^2][(x-p)^2-a^2]}+(W-p)(x-p)-a^2)}\right|, & x > p+a \text{ or } x < p-a, \end{cases} \quad (68)$$

where the positive (negative) sign applies to $x < p-a$ ($x > p+a$). The parameters a and p again are determined by the applied current and field,

$$I_T = \frac{I_c}{2W}\left[\sqrt{(W+p)^2-a^2} - \sqrt{(W-p)^2-a^2}\right] \quad (69)$$

and

$$B_a = (B_f/2)\ln\left[\left\{\sqrt{(W+p)^2-a^2}+W+p\right\}\left\{\sqrt{(W-p)^2-a^2}+W-p\right\}/a^2\right]. \quad (70)$$

It is interesting to note that in this low-current–high-field regime, using the definitions of β and ω and some algebra, we obtain expressions for a and p that are identical to those given by Eqs. (63) and (64) for the high-current–low-field regime. This again is in contrast to the slab case, where the roles of I_T and B_a are interchanged as the current gets smaller. The results obtained for the low-current–high-field regime in thin films are restricted by inequalities that are the reverse of those given in Eqs. (65) and (66). Such a case is depicted in Figs. 9(c) and 9(d).

The magnetization of the thin-film strip in the monotonic case is obtained by integrating the current densities of Eqs. (59) and (67) using Eq. (20). A lengthy integration procedure gives identical results for both the high-current–low-field and low-current–high-field regimes:

$$M_z/M_{\max} = -[1-(I_T/I_c)^2]\tanh(B_a/B_f). \quad (71)$$

At zero current we recover the results of Sec. II. At high fields, however, the current dependence of the magnetization is different from that of Eq. (36). This is because the current distribution in the monotonic case [Fig. 9(c)] is very different from that of the nonmonotonic, remanent initial state case shown in Fig. 4(c).

To our knowledge, no experimental results in the configuration of a monotonic application of field and current have been reported. Conduction of such experiments should be possible using magneto-optic or Hall-sensor techniques.

VII. NONMONOTONIC CASE: SPATIAL VARIATION OF THE CRITICAL-CURRENT DENSITY

We now describe the procedure for determining the current and field distributions in the general case when the field and the transport current are applied in any sequence. The previous sections have dealt with various simple cases to which the current superposition approach can be applied. Here we analyze the case in which a sample, initially in a virgin state, is subjected first to a field B_a and then to a transport current I_T. This is a very common experimental situation, which cannot be solved by the techniques described in the previous sections for the case of a thin-film strip. The procedure developed below can be readily generalized to treat any sequence of applied fields and currents.

As in the previous sections, we start with slab geometry for clarity. In an infinite slab the superposition approach always can be applied, and hence the solution is straightforward. A positive field B_a applied to the slab results in current flowing with critical density on both sides of the slab, and the field-free region extends from $-a_L = -a$ to $a_R = a$, as given by Eq. (7) and as shown in Figs. 2(a) and 2(b). This state is the new initial condition for the application of the transport current. The additional transport current must flow on both sides of the slab, maintaining now a new field-invariant region inside the slab. We denote the width of the new field-invariant region by $2a'$, which spans the region $-a'_L < x < a'_R$. In the case of a positive transport current, half of the added current (per unit height of the slab) flows near the right surface of the slab, where the added current density is $2J_c$, changing the total current density from $-J_c$ to $+J_c$. On the left side of the slab, the current density arising from the magnetic field already is at J_c, and therefore the transport current penetrates deeper into the slab and encroaches on the left side of the original vortex-free region. The resulting total current distribution for positive B_a and I_T is given by

$$J_y(x) = \begin{cases} J_c, & -W < x < -a'_L, \\ 0, & -a'_L < x < a_R, \\ -J_c, & a_R < x < a'_R, \\ J_c, & a'_R < x < W, \end{cases} \tag{72}$$

where $a_R = W(1 - B_a/B_s)$, $a'_R = W(1 - I_T/2I_c)$, and $a'_L = W(1 - B_a/B_s - I_T/I_c)$. This distribution holds as long as the transport current is low enough that $a'_R > a_R$ or $I_T/I_c < 2B_a/B_s$. At higher transport currents the right side of the field-invariant region a'_R passes the right side of the original field-free region a_R, thus erasing the "memory" of a_R. As a result, the distributions become identical to the results of the monotonic case of Eqs. (49) to (51).

Figures 10(a) and 10(b) show the corresponding current-density and field profiles in a slab for $B_a/B_s = 0.4$ and various I_T/I_c values. For $I_T/I_c = 0.9$ the distribution is equivalent to the monotonic case shown in Figs. 8(a) and 8(b), since $a'_R < a_R$. For sufficiently high fields the left side of the field-invariant region $-a'_L$, rather than the right side a'_R, passes a_R as the transport current is increased. This happens when $B_a/B_s > 0.5$ and $I_T/I_c > 2(1 - B_a/B_s)$. Note that there is a fundamental difference between the two cases. In the low-field case, when $a'_R < a_R$, the new field-invariant region is enclosed within the original field-free region, and therefore the trapped flux in the field-invariant region is zero. This situation is equivalent to the monotonic case. At high fields when $-a'_L > a_R$, there is flux trapped in the field-invariant region, and therefore the current density in this region is now $-J_c$ rather than 0. The resulting distributions are similar to the case of the transport current applied to the remanent state shown in Figs. 4(a) and 4(b). In the remanent state, however, the field-invariant region is centered about $\pm W/2$, whereas here the position of the center is determined by the value of B_a/B_s.

In order to analyze the film geometry, we first must understand the limitations of the superposition technique that we have used so far. In the previous section we showed that in order to solve the current distribution for the monotonic case we had to obtain the image current associated with the generating critical current on each edge of the sample separately. The profile of each image-current distribution depends on both the width of the generating current stripe and the width of the field-invariant region, as shown by the last terms on the right-hand sides of Eqs. (57) and (58). The image currents associated with the two generating currents on opposite edges are therefore interdependent, since flux penetration on one side shrinks the field-invariant region and

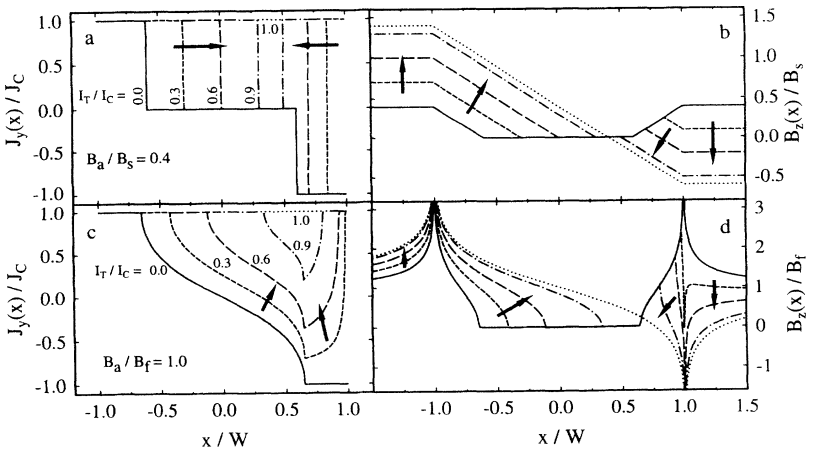

FIG. 10. Calculated critical-state behavior for the nonmonotonic application of field followed by application of transport current. The current-density and magnetic-flux-density profiles for slabs are shown in (a) and (b), and the corresponding profiles for films are shown in (c) and (d). The solid curves show the profiles after the initial application of the magnetic field $B_a = 0.4B_s$ or $B_a = B_f$ with no transport current. Arrows indicate the progression of the subsequent profiles as the transport current I_T is increased.

forces the image current of the opposite side to adjust itself accordingly. Given the functional form of the image currents, the solution of the monotonic case reduces to the problem of finding the values of a_L and a_R that correspond to the applied field and current.

The nonmonotonic case is more complicated because, having established a_L and a_R after some initial monotonic increase of field or current, a nonmonotonic change of the external conditions results in a new flux-front penetration determined by a'_L and a'_R. If each of the new generating currents on the sample edges is in a direction opposite to that of the original generating current, the problem is easily solved. This is, for example, the case for alternating fields or currents described in Sec. V. In addition, the discussion in Sec. VI readily can be extended to deal with such a case. However, if the new generating current is in the same direction on one edge and in a direction opposite to the original current on the other edge of the sample, a new approach is needed.

The current distribution of a thin-film strip exposed to an applied field B_a in the positive z direction is shown by the solid curve in Fig. 10(c). Addition of a small transport current in the positive y direction causes a current reversal at the right edge of the strip at $a'_R < x < W$, but not on the left edge, where a positive generating current now extends from $x = -W$ to $x = -a'_L$. The image current associated with the new generating current on the right edge can be readily found and superimposed onto the original currents. However, using the previous approach we cannot define the new image current due to the total generating current on the left edge. The difficulty is the increase of the width of the field-invariant region. If we use the image current given by the last term of Eq. (57) with the field-invariant region $-a'_L < x < a_R$, we preserve the original field profile in this region. However, the field is changed in the region $a_R < x < a'_R$, where it should be invariant as well. If the image current is calculated for $-a'_L < x < a'_R$, then the field profile will be invariant under further variations of a'_L or a'_R but will not be equal to the original field profile, which had a sharp change in slope at $x = a_R$. Equation (57) is simply invalid in this case.

The proposed approach, which we denote as the "spatial variation of the critical current" method, is as follows. The additional transport current may flow only in the regions for which $J_{0y}(x) < J_c$, where $J_{0y}(x)$ is the current distribution from the originally applied field as given by Eq. (17). We therefore may replace the "original sample" by a "new sample" in which $J'_c(x) = J_c - J_{0y}(x)$ is the maximum available distribution for the flow of the transport current. We thus regard $J'_c(x)$ as the spatially dependent critical current of the new sample. This critical current is shown in Fig. 11 by the solid curve. Hence, we have reduced the problem of nonmonotonic experimental conditions to the problem of piecewise monotonic segments in which the final conditions of the previous segment define the new $J'_c(x)$ of the next segment. The procedure of Sec. VI has to be repeated now for the case of spatial variation of the critical-current density.

For the flux penetration from the right the associated image current is given by twice the last term of Eq. (58), since $J'_c(x)$ at the right edge is just $2J_c$ (for $a'_R > a_R = a$). The left-side contribution is given by an integral similar to that in Eq. (57),

$$\frac{-1}{\pi\sqrt{1-x'^2}}\int_1^{W'_L} J'_c(p'-ta')\frac{\sqrt{t^2-1}}{t+x'}dt\ , \tag{73}$$

where

$$J'_c(p'-ta') = J_c\left[1+\frac{2}{\pi}\arctan\left(\frac{(p'-ta')}{W}\sqrt{\frac{W^2-a^2}{a^2-(p'-ta')^2}}\right)\right], \tag{74}$$

$W'_L = (a+p')/a'$, $p' = (a'_R - a'_L)/2$, and $a' = (a'_R + a'_L)/2$. To the best of our knowledge there is no analytical solution to this integral and it has to be evaluated numerically. The procedure is further complicated by the fact that the result includes diverging terms like those in Eq. (57) which are not part of the desired solution.

It can be shown that the continuous part of the solution of Eq. (73), which is the desired image current, can be well approximated by the following function, so that the current distribution in the "new sample" is given by

$$J'_y(x) \simeq \begin{cases} 0, & -W < x \le -a, \\ J_c\left[1+\frac{2}{\pi}\arctan\left(\frac{x}{W}\sqrt{\frac{W^2-a^2}{a^2-x^2}}\right)\right], & -a < x \le -a'_L, \\ \frac{J_c}{\pi}\left[\arcsin\frac{(x+a-a_m)(a_m+\delta)+a_m^2}{a_m(x+a+\delta)} - \arcsin\frac{(x-p')(p'+a+\delta)+a'^2}{a'(x+a+\delta)}\right. & \\ \quad \left. + \arcsin\frac{x+a-a_m}{a_m} - \arcsin\frac{x-p'}{a'} + \pi + 2\arcsin\frac{(x-p')(W-p')-a'^2}{a'(W-x)}\right], & -a'_L < x < a'_R, \\ 2J_c, & a'_R \le x < W, \end{cases} \tag{75}$$

where $a_m = (a + a'_R)/2$ and the value of the parameter δ is adjusted to provide continuity of the current distribution at $x = -a'_L$. The last two terms of the current-distribution expression in the field-invariant region, $-a'_L < x < a'_R$, are the image current associated with the generating current on the right edge, whereas the remaining terms are the approximate nondivergent part of the solution of Eq. (73).

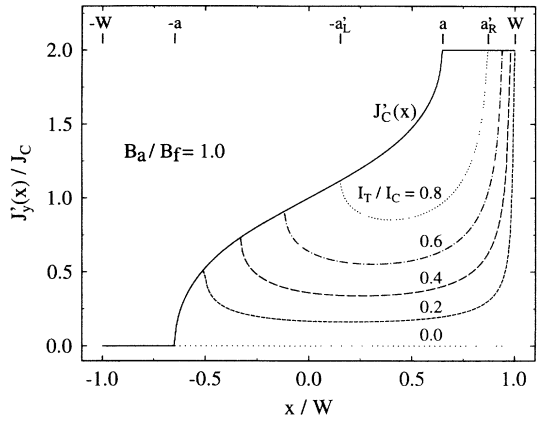

FIG. 11. Calculated added current profiles $J'_y(x)$ in the case of nonmonotonic application of a field, followed by the application of a transport current in thin-film geometry. The solid curve shows the spatial dependence of the available critical-current density after the initial application of the field $B_a = B_f$. The rest of the curves show the added current profiles as I_T is increased from 0 to $0.8I_c$. At $I_T = I_c$ the added current distribution equals $J'_c(x)$. The delimiters at the top show the position of the various parameters for the case of $B_a = B_f$ and $I_T = 0.8I_c$.

As in the monotonic case the parameters a'_R and a'_L (or a' and p') determine the magnitude of the uniform field in the $-a'_L < x < a'_R$ region and the total current carried by the strip. Since we require field invariance, the first constraint on a'_L and a'_R is that the magnetic field arising from $J'_y(x)$ be zero in the field-invariant region $-a'_L < x < a'_R$. The second constraint is that the total current of the strip arising from $J_{0y}(x)$ and $J'_y(x)$ be equal to the applied transport current. Since in our particular case the current carried by $J_{0y}(x)$ is zero, this requirement reduces to the constraint that the integral of $J'_y(x)$ over the cross section of the film equals I_T. Using these conditions, a'_L and a'_R can be readily evaluated numerically. The resulting $J'_y(x)$ profiles are shown in Fig. 11 for the various values of I_T/I_c. Figure 10(c) shows the profiles of the total current density $J_y(x) = J_{0y}(x) + J'_y(x)$ in the film, and the corresponding field $B_z(x)$ is presented in Fig. 10(d).

As in the case of slab geometry, Eq. (75) holds only if $a'_R > a$ and $-a'_L < a$. If either edge of the new field-invariant region crosses the right edge of the original field-free region a, Eq. (75) has to be modified. If a'_R becomes smaller than a, we may continue to use the same $J'_c(x)$ approach. However, in our particular case it is more convenient to return to the "original sample" since the current and field profiles become identical to Eqs. (59) and (60) with the field-free region parameters given by Eqs. (63) and (64). We may determine the conditions for such a crossing by equating a of Eq. (15) to $a_R = p + a$ determined from Eqs. (63) and (64), which gives

$$\frac{I_T}{I_c} = \frac{2\sinh(B_a/B_f)}{1+\sinh^2(B_a/B_f)}. \tag{76}$$

At low fields, such that $\operatorname{arcsinh}(B_a/B_f) < 1$ or $B_a/B_f < 0.88$, a'_R crosses a if the current is raised above a value determined by Eq. (76). At high fields, a'_L will be the one that passes a at high enough transport current. If $B_a/B_f = 0.88$, both edges of the new field-invariant region merge at $x = a = W/\sqrt{2}$ at $I_T = I_c$. Note that once I_T/I_c exceeds the condition of Eq. (76), the current distribution is given by Eq. (59) only in the low-field case. Figures 10(c) and 11 present the current distributions for the particular case of $B_a/B_f = 1$, only slightly higher than 0.88, which is the reason for not observing the crossing for the presented I_T/I_c values. In this case $-a'_L$ crosses a at I_T very close to I_c, as can be seen in Fig. 10(d) by the fact that the field profile at $I_T/I_c = 1.0$ intersects the original profile to the right of $x = a$.

In order to derive the current distributions for the high-field case when $-a'_L > a$, we must continue to use the $J'_c(x)$ approach as described above. The approximation to the solution of Eq. (73) as given in Eq. (75) works poorly, however, for the case of $B_a/B_f > 1$. On the other hand, in this case, $J'_c(x)$ can be well approximated by a third-order polynomial. In this approximation Eq. (73) can be solved analytically as described in the Appendix. Figures 12(c) and 12(d) show the resulting total current and field profiles for $B_a/B_f = 2.0$ and various transport currents. It is interesting to compare, for example, the $I_T/I_c = 0.9$ current and field profiles in the thin-film strip as shown in Figs. 8, 10, and 12. In all three cases the generating currents on both sides of the

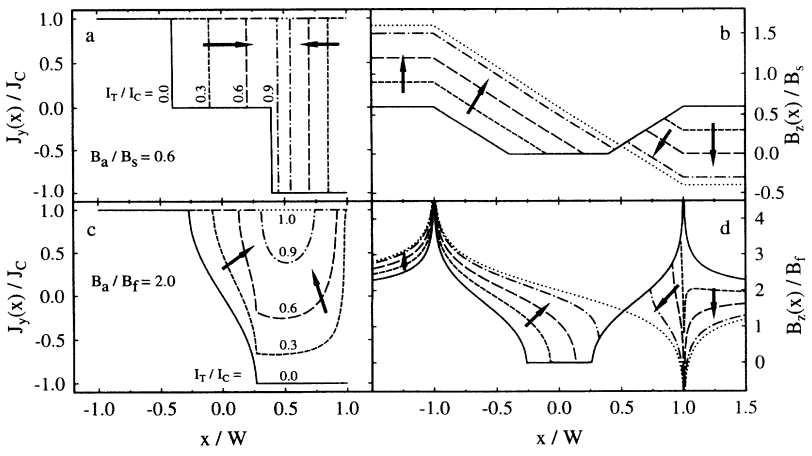

FIG. 12. Calculated critical-state behavior for the nonmonotonic application of a field followed by the application of a transport current. The current-density and magnetic-flux-density profiles for slabs are shown in (a) and (b), and the corresponding profiles for films are shown in (c) and (d). The solid curves show the profiles after the initial application of the magnetic field $B_a = 0.6B_s$ or $B_a = 2B_f$ with no transport current. Arrows indicate the progression of the subsequent profiles as the transport current I_T is increased.

field-invariant region are basically the same. However, the associated image currents are very different. This is the result of the presence of trapped flux in the field-invariant region. In the monotonic case of Fig. 8 the trapped flux is zero, and $B_z(x) = 0$ in the field-invariant region in Fig. 8(d). In the nonmonotonic case of Fig. 10 the new field-invariant region partially overlaps the original vortex-free region, and therefore only the right side of the field-invariant region includes trapped vortices, as seen by the field profile in Fig. 10(d). In Fig. 12 at $I_T/I_c = 0.9$ the entire field-invariant region encapsulates trapped flux. The image current derivation as proposed by Norris[23] is correct only if there is no flux trapped in the field-invariant region. The results of Secs. II – VI were obtained either for the case of zero trapped flux or for cases where superposition could be used, such that the superimposed generating currents are equal to $\pm J_c$. As shown above, in the general case, the $J_c'(x)$ approach has to be used instead.

As a final example of this technique, we analyze the nonmonotonic case in which a transport current is driven first through a thin-film strip and then an additional magnetic field is applied. The initial transport-current distribution $J_{0y}(x)$ is given by Eq. (27) and shown by the solid curve in Fig. 13(c). When the magnetic field is applied, positive generating currents flow at the left edge of the film, whereas negative generating currents flow on the right edge. Therefore, as a general rule in the nonmonotonic case, we have to introduce a new critical-current density for positive generating currents, $J_c^p(x) = J_c - J_{0y}(x)$, and a new negative critical-current density for negative generating currents, $J_c^n(x) = J_c + J_{0y}(x)$, which are not equal, as shown by the two solid curves in Fig. 14. We now have to find the image currents associated with each of the new generating currents. At fields low enough such that $a_R' > a$ the negative image current of the right edge is twice that of the last term of Eq. (58) since the generating current is uniform and equal to $-2J_c$. To obtain the image current associated with the left edge we again have to integrate Eq. (73) but with $J_c^p(t)$ given by

$$J_c^p(p'-ta') = J_c\left[1 - \frac{2}{\pi}\arctan\sqrt{\frac{W^2-a^2}{a^2-(p'-ta')^2}}\right]. \tag{77}$$

Since we are interested only in the continuous terms, the solution can be well approximated (up to $I_T/I_c \simeq 0.8$) by

$$J_y'(x) \simeq \begin{cases} 0, & -W < x \le -a, \\ J_c\left[1 - \frac{2}{\pi}\arctan\sqrt{\frac{W^2-a^2}{a^2-x^2}}\right], & -a < x \le -a_L', \\ \frac{J_c}{\pi}\left[\arcsin\frac{(x+a-a_m)(a_m+\delta)+a_m^2}{a_m(x+a+\delta)} - \arcsin\frac{(x-p')(p'+a+\delta)+a'^2}{a'(x+a+\delta)}\right. & \\ \quad - \arcsin\frac{(x+a-a_m)(W+a_m-a)-a_m^2}{a_m(W+a_R'-a-x)} + \arcsin\frac{(x-p')(W+a'-a)-a'^2}{a'(W+a_R'-a-x)} & \\ \quad \left. -\pi - 2\arcsin\frac{(x-p')(W-p')-a'^2}{a'(W-x)}\right], & -a_L' < x < a_R', \\ -2J_c, & a_R' \le x < W, \end{cases} \tag{78}$$

where the parameter δ is used to provide continuity of the current at $x = -a_L'$. The resulting $J_y'(x)$ profiles are shown in Fig. 14 for the various B_a/B_f ratios. Figure 13(c) describes the total current distribution in the sample, and the corresponding field profiles are shown in Fig. 13(d).

As the field is increased, the right edge of the field-invariant region a_R' approaches the edge of the original field-free region a and passes it when

$$\cosh(B_a/B_f) > \frac{1}{1-2(I_T/I_c)^2}, \tag{79}$$

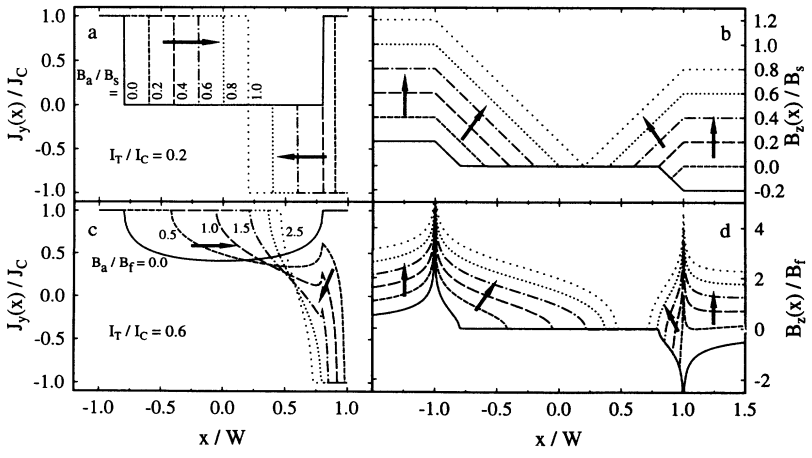

FIG. 13. Calculated critical-state behavior for the nonmonotonic application of a transport current followed by the application of a magnetic field. The current-density and magnetic-flux-density profiles for slabs are shown in (a) and (b), and the corresponding profiles for films are shown in (c) and (d). The solid curves show the profiles after the initial application of the transport current $I_T = 0.2I_c$ for slab geometry and $I_T = 0.6I_c$ for film geometry in the absence of an applied field. Arrows indicate the progression of the subsequent profiles as the applied field is increased.

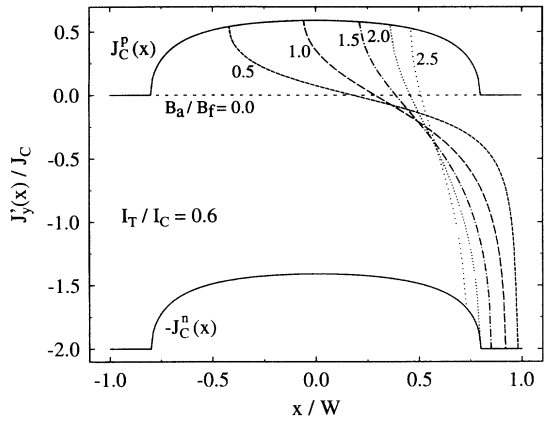

FIG. 14. Calculated added current profiles $J_y'(x)$ in the case of nonmonotonic application of transport current followed by the application of a magnetic field in thin-film geometry. The solid curves show the available critical-current-density profiles for generating currents flowing in the positive y direction, $J_c^p(x)$, and in the negative direction, $J_c^n(x)$, following the initial application of $I_T = 0.6I_c$. The remaining curves show the added current profiles as B_a is increased from 0 to $2.5B_f$.

which happens at $B_a/B_f \simeq 2$ in the case of Fig. 14. From this point on the total current distribution, $J_y(x) = J_{0y}(x) + J_y'(x)$, becomes identical to that of the monotonic case described by Eqs. (67), (63), and (64) because no more trapped flux remains in the field-invariant region, as seen in Fig. 13(d). If the original transport current I_T is larger than $I_c/\sqrt{2}$, on the other hand, the left edge of the new field-invariant region reaches $x = a$ at high enough fields that trapped vortices exist in the entire field-invariant region. In this case a better approximation may be obtained by an even-power polynomial fit of $J_c^p(x)$ using the procedure outlined in the Appendix.

To our knowledge, no experimental results in the configuration of a nonmonotonic application of field and current have been reported. Conduction of such experiments should be possible using magneto-optic or Hall-sensor techniques.

VIII. SUMMARY

We have presented a general approach for the description of current and field profiles in a type-II superconducting thin-film strip carrying a transport current in the presence of applied fields. As the fields or currents are changed, vortices penetrate (or exit) through the edges of the sample, thus defining flux-penetrated regions next to the edges and a field-invariant region in the central part of the strip. In the flux-penetrated regions the magnitude of the current density equals the critical-current density J_c. In the field-invariant region we find a continuous distribution of currents that may vary in density from $-J_c$ to J_c, in sharp contrast to the behavior when the Bean model[16,17] is applied to an infinite slab.

If the entire field-invariant region is vortex free, we have shown that the method proposed by Norris[23] for calculating the transport currents can be extended to treat the effects of an applied field. In this method the image currents in the field-invariant region, calculated by use of conformal mapping, take into account both the generating currents in the flux-penetrated regions and the changing width of the field-invariant region. We also presented some additional cases, including an alternating field in the absence of a transport current, an alternating current with no applied field, and the simultaneous monotonic application of field and current, which also can be calculated by use of superposition and symmetry arguments. However, a general nonmonotonic situation cannot be adequately described in this manner because the presence of trapped flux in the field-invariant region severely complicates the determination of the image currents induced by the generating currents.

Our novel approach for solving the nonmonotonic case is based on dividing the time sequence of the applied field and current into a series of monotonic segments. The final current distribution of each time segment, $J_{0y}(x)$, determines the remaining current-density distributions, $J_c^p(x) = J_c - J_{0y}(x)$ and $J_c^n(x) = J_c + J_{0y}(x)$, available for screening of the deviations in the applied field or current in the next segment relative to the final conditions of the previous segment. The additional image currents of the new segment are now calculated using the new effective spatially varying critical currents $J_c^p(x)$ and $J_c^n(x)$. Two particular cases, transport current applied after magnetic field and field applied after transport current, are solved in detail in order to demonstrate the feasibility of the technique.

The obtained results have important consequences on the interpretation of experimental data. In a thin film the flux penetration depth is a nonlinear function of the applied field and applied transport current in contrast to the slab geometry. This has a profound effect on the dc magnetization behavior, including the apparent first penetration, as well as ac response and losses.[34] In addition, the fact that there is a continuous nonuniform current distribution in the sample at any field or current should have a significant effect on the relaxation behavior as well as I-V characteristics. In particular, if the applied field or transport current is slightly reduced, the resulting current distribution becomes less than critical in most of the volume of the film, which thereby drastically reduces the relaxation rate, as recently observed.[9]

The method of "spatial variation of critical current" introduced in Sec. VII for solving the nonmonotonic cases can be directly applied to situations in which the real critical-current density is nonuniform. Such nonuniformity of J_c may arise from defects, field dependence of the critical current, edge pinning, or nonuniform thickness of the thin film. In addition, although the presented analysis describes the current and field distributions in thin films, the obtained results may provide important insight into the behavior of thicker samples, such as single crystals of high-T_c superconductors, which in perpendicular fields are geometrically more similar to thin films than to infinite slabs. Finally, our analysis should be applicable to the calculation of ac losses in the flat filaments of multifilamentary $Bi_2Sr_2Ca_2Cu_3O_x$/Ag composite tapes.

In the final stages of preparation of this manuscript we received a report[25] by Brandt and Indenbom, who used similar methods to solve a number of the same problems treated above in Secs. II–VI. To the extent that the treatments overlap, our results are in general agreement with Ref. 25 except for a few minor differences in notation. Our work, however, contains a number of solutions not obtained in Ref. 25, in particular the general case when the field and transport current are applied in any sequence (Sec. VII).

ACKNOWLEDGMENTS

We thank E. H. Brandt, M. Indenbom, J. Lockhart, J. Sun, J. Zhu, V. B. Geshkenbein, and A. I. Larkin for helpful discussions and correspondence. This work was supported by a grant from the Philip M. Klutznick Fund for Research in Weizmann Institute of Science and by the Israeli Ministry of Science and Technology under Contract No. 3759-1-91. Ames Laboratory is operated for the U.S. Department of Energy by Iowa State University under Contract No. W-7405-Eng-82. This research was supported by the Director for Energy Research, Office of Basic Energy Sciences, by the Midwest Superconductivity Consortium (MISCON) through DOE Grant No. DE-FG02-90ER45427, and by the Electric Power Research Institute. The work at Purdue was also supported by MISCON.

APPENDIX

A nonmonotonic change of applied field or current generally results in a new flux front penetrating into the sample and a new field-invariant region. In order to determine the resulting distribution of current in thin-film geometry, it is necessary to determine the integral of Eq. (73) for the left edge of the sample and a similar integral for the right edge. In the particular nonmonotonic case in which the sample is first exposed to a magnetic field and the transport current is next applied, the result given by Eq. (75) is a good approximation for relatively low field values such that $B_a/B_f < 1$. At higher fields a more accurate result is obtained by use of the following polynomial approximation for $J_c'(x)$:

$$J_c'(x) = J_c\left[1+\frac{2}{\pi}\arctan\left(\frac{x}{W}\sqrt{\frac{W^2-a^2}{a^2-x^2}}\right)\right] \simeq J_c(1+\eta x+\nu x^3), \quad -a<x<a, \tag{A1}$$

where the parameters η and ν are chosen to obtain the best fit in the range $-a < x < a$. For such a polynomial Eq. (73) can be calculated analytically. At low transport currents such that $-a_L' < a$, the resulting continuous current distribution is given by

$$J_y'(x) \simeq \begin{cases} 0, & -W < x \le -a, \\ J_c\left[1+\frac{2}{\pi}\arctan\left(\frac{x}{W}\sqrt{\frac{W^2-a^2}{a^2-x^2}}\right)\right], & -a < x \le -a_L', \\ \frac{J_c}{\pi}\Bigg((1+\eta x+\nu x^3)\left(\frac{\pi}{2}-\arcsin\frac{(x-p')(p'+a)+a'^2}{a'(x+a)}\right) & \\ \quad -\sqrt{a'^2-(x-p')^2}\Big\{(\eta+\nu p'^2+\nu a'^2/2+\nu p' x+\nu x^2)\ln\left[\sqrt{\left(\frac{p'+a}{a'}\right)^2-1}+\frac{p'+a}{a'}\right] & \\ \quad +\nu(a/2-3p'/2-x)\sqrt{(p'+a)^2-a'^2}\Big\}+\pi+2\arcsin\frac{(x-p')(W-p')-a'^2}{a'(W-x)}\Bigg), & -a_L' < x < a_R', \\ 2J_c, & a_R' \le x < W, \end{cases} \tag{A2}$$

where the last two terms of the expression in the field-invariant region $-a_L' < x < a_R'$ are the result of the image current associated with the constant generating currents, $2J_c$, at the right-edge of the film.

At higher transport currents such that $-a_L' > a$ we may write Eq. (73) in the form

$$\frac{-J_c}{\pi\sqrt{1-x'^2}}\left[2\int_1^{(p'-a)/a'}\frac{\sqrt{t^2-1}}{t+x'}dt+\int_{(p'-a)/a'}^{(p'+a)/a'}J_c'(p'-ta')\frac{\sqrt{t^2-1}}{t+x'}dt\right]. \tag{A3}$$

Keeping only the continuous terms and adding the right-edge current we obtain

$$J_y'(x) \simeq \begin{cases} 0, & -W < x \le -a, \\ J_c\left[1+\frac{2}{\pi}\arctan\left(\frac{x}{W}\sqrt{\frac{W^2-a^2}{a^2-x^2}}\right)\right], & -a < x < a, \\ 2J_c, & a \le x \le -a_L', \\ \frac{J_c}{\pi}\Big\{(1+\eta x+\nu x^3)\left(\arcsin\frac{(x-p')(p'-a)+a'^2}{a'(x-a)}-\arcsin\frac{(x-p')(p'+a)+a'^2}{a'(x+a)}\right) & \\ \quad -\sqrt{a'^2-(x-p')^2}\Big[(\eta+\nu p'^2+\nu a'^2/2+\nu p'x+\nu x^2)\ln\frac{\sqrt{(p'+a)^2-a'^2}+p'+a}{\sqrt{(p'-a)^2-a'^2}+p'-a} & \\ \quad +\nu(a/2-3p'/2-x)\sqrt{(p'+a)^2-a'^2}+\nu(a/2+3p'/2+x)\sqrt{(p'-a)^2-a'^2}\Big] & \\ \quad +2\pi-2\arcsin\frac{(x-p')(p'-a)+a'^2}{a'(x-a)}+2\arcsin\frac{(x-p')(W-p')-a'^2}{a'(W-x)}\Big\}, & -a_L' < x < a_R', \\ 2J_c, & a_R' \le x < W, \end{cases} \tag{A4}$$

The a_L' and a_R' can be readily obtained numerically by requiring that the field arising from $J_y'(x)$ in the field-invariant region be zero and that the total current arising from $J_y'(x)$ be equal to I_T. In a more general case, in which $J_{0y}(x)$ is determined by a monotonic increase of the field and current to some value B_{a1} and I_{T1}, and $J_y'(x)$ is determined by some nonmonotonic direction reversal and subsequent monotonic approach to B_{a2} and I_{T2}, the a_L' and a_R' are obtained from the condition that $J_y'(x)$ carries a current of $I_{T2}-I_{T1}$ and produces a field of $B_{a1}-B_{a2}$ in the new field-invariant region.

[1] H. Theuss, A. Forkl, and H. Kronmuller, Physica C **190**, 345 (1992).
[2] L. A. Dorosinskii, M. V. Indenbom, V. I. Nikitenko, Yu. A. Ossip'yan, A. A. Polyanskii, and V. K. Vlasko-Vlasov, Physica C **203**, 149 (1992).
[3] C. A. Duran, P. L. Gammel, R. Wolfe, V. J. Fratello, D. J. Bishop, J. P. Rice, and D. M. Ginsberg, Nature **357**, 474 (1992).
[4] V. K. Vlasko-Vlasov, M. V. Indenbom, V. I. Nikitenko, V. I. Nikitenko, A. A. Polyanskii, R. L. Prozorov, I. V. Grekhov, L. A. Delimova, I. A. Liniichuk, A. V. Antonov, and M. Yu. Gusev, Superconductivity **5**, 1582 (1992).
[5] M. V. Indenbom, A. Forkl, H. U. Habermeier, and H. Kronmuller, J. Alloys Compounds **195**, 499 (1993).
[6] M. Konczykowski, F. Holtzberg, and P. Lejay, Supercond. Sci. Technol. **4**, 8331 (1991).
[7] M. Konczykowski, L. I. Burlachkov, Y. Yeshurun, and F. Holtzberg, Phys. Rev. B **43**, 13 707 (1991).
[8] D. A. Brawner, A. Schilling, H. R. Ott, R. J. Haug, K. Ploog, and K. von Klitzing, Phys. Rev. Lett. **71**, 785 (1993).
[9] M. Darwin, J. Deak, L. Hou, M. McElfresh, E. Zeldov, J. R. Clem, and M. Indenbom, Phys. Rev. B **48**, 13 192 (1993).
[10] D. A. Brawner and N. P. Ong, J. Appl. Phys. **73**, 3890 (1993).
[11] T. Tamegai, Y. Iye, I. Oguro, and K. Kishio, Physica C **213**, 33 (1993).
[12] A. M. Chang, H. D. Hallen, L. Harriott, H. F. Hess, H. L. Kao, J. Kwo, R. E. Miller, R. Wolfe, J. van der Ziel, and T. Y. Chang, Appl. Phys. Lett. **61**, 1974 (1992).
[13] T. Tamegai, L. Krusin-Elbaum, P. Santhanam, M. J. Brady, W. T. Masselink, C. Feild, and F. Holtzberg, Phys. Rev. B **45**, 2589 (1992).
[14] S. T. Stoddart, H. I. Mutlu, A. K. Geim, and S. J. Bending, Phys. Rev. B **47**, 5146 (1993).
[15] E. Zeldov *et al.* (unpublished).
[16] C. P. Bean, Phys. Rev. Lett. **8**, 250 (1962).
[17] A. M. Campbell and J. E. Evetts, Adv. Phys. **21**, 199 (1972).
[18] J. R. Clem, J. Appl. Phys. **50**, 3518 (1979).
[19] D. J. Frankel, J. Appl. Phys. **50**, 5402 (1979).
[20] M. Daumling and D. C. Larbalestier, Phys. Rev. B **40**, 9350 (1989).
[21] L. W. Conner and A. P. Malozemoff, Phys. Rev. B **43**, 402 (1991).
[22] L. W. Conner, A. P. Malozemoff, and I. A. Campbell, Phys. Rev. B **44**, 403 (1991).
[23] W. T. Norris, J. Phys. D **3**, 489 (1970).
[24] E. H. Brandt, M. Indenbom, and A. Forkl, Europhys. Lett. **22**, 735 (1993).
[25] E. H. Brandt and M. Indenbom, Phys. Rev. B **48**, 12 893 (1993).
[26] G. W. Swan, J. Math. Phys. **9**, 1308 (1968).
[27] R. P. Huebener, R. T. Kampwirth, and J. R. Clem, J. Low Temp. Phys **6**, 275 (1972).
[28] J. Pearl, in *Proceedings of the Ninth International Conference on Low Temperature Physics*, edited by J. G. Daunt, D. V. Edwards, F. J. Milford, and M. Yaqub (Plenum, New York, 1965), Pt. A, p. 566; J. Pearl, Appl. Phys. Lett. **5**, 65 (1964).
[29] P. G. deGennes, *Superconductivity of Metals and Alloys* (Benjamin, New York, 1966).
[30] A. I. Larkin and Yu. N. Ovchinnikov, Zh. Eksp. Teor. Fiz. **61**, 1221 (1971) [Sov. Phys. JETP **34**, 651 (1972)].
[31] V. B. Geshkenbein and A. I. Larkin (private communication).
[32] P. N. Mikheenko and Yu. E. Kuzovlev, Physica C **204**, 229 (1993).
[33] J. Zhu, J. Mester, J. Lockhart, and J. Turneaure, Physica C **212**, 216 (1993).
[34] J. R. Clem and A. Sanchez (unpublished).